

## Theory, Simulation, and Experiments on a Magnetically Insulated Line Oscillator (MILO) at 10 kA, 240 kV Near Hull Cutoff Condition

Drew A. Packard,<sup>1, a)</sup> Y. Y. Lau,<sup>1</sup> E. N. Guerin,<sup>1</sup> C. J. Swenson,<sup>1</sup> S. V. Langellotti,<sup>1</sup> A. Jassem,<sup>1</sup> D. Li,<sup>1</sup> N. M. Jordan,<sup>1</sup> J. W. Luginsland,<sup>2</sup> R. D. McBride,<sup>1</sup> and R. M. Gilgenbach<sup>1</sup>

<sup>1</sup>*Nuclear Engineering and Radiological Sciences, University of Michigan, Ann Arbor, Michigan 48109, USA*

<sup>2</sup>*Air Force Office of Scientific Research, Arlington, VA 22201, USA*

(Dated: 5 November 2021)

The magnetically insulated line oscillator (MILO) is a high power microwave source that has received increased attention recently because it does not require an external magnetic field. Self-magnetic insulation typically requires operation at high currents,  $\sim 50$  kA in previous experiments (at  $\sim 10 \Omega$ ). This paper reports the first MILO experiment operating at moderate current, less than 10 kA, at a lower voltage of 240 kV, driven by the Michigan Electron Long Beam Accelerator (MELBA). The viability of this lower current operation was predicted by our recently developed theory on Brillouin flow, which also led to the rigorous derivation, for the first time, of the Buneman-Hartree condition for the cylindrical MILO using both the Brillouin flow and single particle model. The experiments show more than 90% of shots operate at a magnetic field less than 1.3 times the Hull-cutoff magnetic field, and this magnetic field is significantly lower than the magnetic field required at the Buneman-Hartree condition. These experiments also oscillated at less current than the Hull cutoff condition on over 80% of shots, suggesting that MILOs might operate at a current lower than that expected at exactly Hull cutoff; this peculiar feature was also predicted by the theory. Particle-in-cell simulations from the ICEPIC and CST codes are detailed, which corroborate MILO operation at lower currents than the Hull cutoff condition. The maximum efficiency achieved in these experiments is 1%, at a resonant frequency of 1 GHz. An initial comparison of the newly developed theory against prior MILO experiments is presented.

### I. INTRODUCTION

Relativistic magnetrons (RMs)<sup>1</sup> and magnetically insulated line oscillators (MILOs)<sup>2-4</sup> are both crossed-field high power microwave (HPM) sources<sup>5-7</sup> capable of generating gigawatts of power. The magnetic field in RMs is provided by an external magnet or solenoid. In a MILO, an external magnetic field is not required. Its magnetic field is generated by the currents flowing primarily along the conducting surfaces of the device as well as in the streaming electrons between the electrodes. Thus, a MILO could operate with a substantial reduction in size and weight relative to a comparable RM. This system advantage has stimulated an intense interest in MILO research over the last decade, despite the low total efficiencies achieved in MILOs (often 4-6%)<sup>8-11</sup> relative to RMs (often 20-50%)<sup>12,13</sup>.

Since magnetic insulation, which is governed by the Hull cutoff condition<sup>14</sup>, is required for both RM and MILO operation, the absence of an external magnetic field necessarily requires a high current for MILO operation. Thus, MILOs typically operate in the range of 50-60 kA, at voltages on the order of 500 kV<sup>4,8-11,15-19</sup>. In this paper, the first MILO experiments operating with a moderate current, of less than 10 kA, are presented. The operating voltage is 240 kV, driven by the Michigan Electron Long Beam Accelerator (MELBA)<sup>20</sup>. Reduced current requirements could enable operation of MILOs with more compact pulsed power. Repetitive operation of HPM devices<sup>21,22</sup> would also benefit from operation at higher impedance and lower current, resulting in less damage to the

hardware.

Using moderate currents to operate a MILO is found feasible in our recent theory on Brillouin flow<sup>23</sup>. This theory is very general. It is applicable to multiple crossed-field geometries, including planar<sup>24</sup> and cylindrical magnetrons<sup>25</sup>, planar and cylindrical MILOs, and radial magnetically insulated transmission lines<sup>26</sup>. For the cylindrical MILO under study, Brillouin flow is in the axial direction, and the magnetic field (which includes the self-magnetic field due to the electrons' motion in the Brillouin flow) is in the azimuthal direction; this theory gives the Buneman-Hartree condition for a cylindrical MILO, rigorously derived from first principles, for the first time. This theory not only predicts that MILOs can operate at a moderate current, such as 10 kA, but also reveals that the self-magnetic field of the Brillouin flow electrons quickly diminishes as the diode is insulated slightly beyond Hull cutoff. The majority of the self-magnetic field is generated by current flow on the cathode surface, even near Hull cutoff, although the Brillouin flow contributes an increasing fraction of insulation as the voltage is increased. Another unexpected result of this theory is that magnetic insulation can be achieved at a lower current than that required for Hull cutoff. The MELBA experiments also definitively reveal a distinctive feature of MILOs, namely, MILOs operate much closer to the Hull cutoff than to the Buneman-Hartree condition, while the converse is true for RMs. These features will be described in this paper.

The theory used to design the experiments and interpret the results is discussed in Section II. Section III details the electromagnetic particle-in-cell simulation results. Section IV describes the experimental configuration. Section V presents the experimental results and their comparison with the newly developed theory. Also included is a similar comparison with prior MILO experiments. Concluding remarks are given in

<sup>a)</sup>Corresponding author: drupac@umich.edu

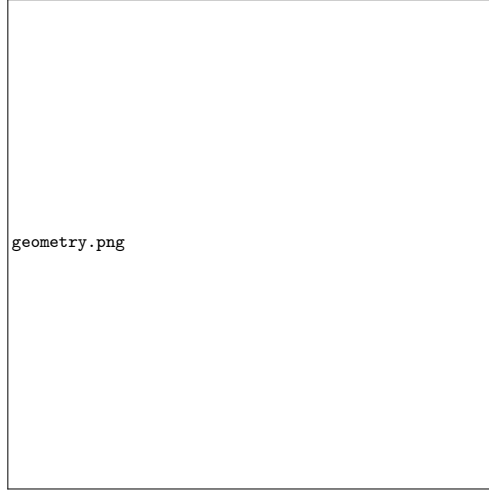


FIG. 1. The cylindrically symmetric coaxial diode with axial flow contains a central cathode of radius  $r_c$  biased at voltage  $-V_a$ , and surrounding, grounded anode of radius  $r_a$ . The resulting electric and magnetic fields are radial and azimuthal, giving rise to Brillouin flow with hub radius  $r_b$  and shear electron velocity in the  $+z$  direction. The anode surface current  $I_a$ , which is the total input current, is defined to flow in the  $+z$  direction, while the cathode surface current  $I_c$  and electron hub current  $I_e$  are anti-parallel to the anode current. The theory<sup>23</sup> considers the smoothbore geometry shown here, but in practice a slow wave structure is implemented on the anode surface.

## Section VI.

## II. THEORY

The recent theory by Lau, et al.<sup>23</sup> describing Brillouin flow in the coaxial geometry with axial flow provided a critical underpinning to the design and analysis of the MILO experiments presented herein. A brief summary of the key equations relevant to the MILO design is given here. Expanded derivations of the equations are available in Ref. 23 and Ref. 27.

The Brillouin flow model for the coaxial MILO assumes a cathode of radius  $r_c$  and anode of radius  $r_a$  ( $> r_c$ ), depicted in Fig. 1. The electrons in the Brillouin hub extend from  $r_c$  to the edge radius  $r_b$ . The theory assumes a smoothbore geometry, so the anode vane inner radius defines  $r_a$ . The Brillouin flow, which is a laminar shear flow in the  $z$ -direction between  $r_c$  and  $r_b$ , is completely characterized by two parameters: the anode voltage  $V_a$ , and the magnetic flux within the AK gap per unit axial length,  $A_a$ . These quantities are normalized by voltage scale  $V_s$  and flux scale  $A_s$ , denoted with a bar,

$$\bar{V}_a = V_a/V_s = V_a e/(mc^2) \quad (1a)$$

$$\bar{A}_a = A_a/A_s = A_a e/(mc) \quad (1b)$$

where  $m$ ,  $e$ , and  $c$  are the electron rest mass, elementary charge, and speed of light, respectively.

From  $\bar{V}_a$ , the relativistic factors  $\beta_a$ ,  $\gamma_a$ , and  $\bar{A}_a^{min}$  may first be constructed,

$$\gamma_a = \bar{V}_a + 1 \equiv 1/\sqrt{1 - \beta_a^2} \quad (2)$$

$$\bar{A}_a^{min} = \gamma_a \beta_a \quad (3)$$

noting that  $\bar{A}_a^{min}$  is the minimum normalized magnetic flux required for magnetic insulation (Hull cutoff). That is, magnetic insulation requires the *flux ratio*, or the fraction,

$$f \equiv \bar{A}_a/\bar{A}_a^{min} > 1. \quad (4)$$

This flux ratio,  $f$ , is roughly equal to the ratio of the magnetic field to the Hull cutoff magnetic field<sup>23</sup>. The Brillouin hub completely fills the anode cathode gap for  $f = 1$ , and recedes to a smaller fraction as the flux ratio is increased.

Together with a specification of the normalized magnetic flux,  $\bar{A}_a$ , (or, equivalently, a specification of the degree of magnetic insulation,  $f$ , as shown in Fig. 2), two auxiliary parameters,  $\chi_b$  and  $\kappa$ , may be constructed,

$$\chi_b = \tanh^{-1} \left( \frac{\gamma_a \bar{A}_a - \sqrt{\bar{A}_a^2 - (\bar{A}_a^{min})^2}}{\bar{A}_a^2 + 1} \right) \quad (5)$$

$$\kappa = \chi_b + \frac{\bar{V}_a - (\cosh \chi_b - 1)}{\sinh \chi_b} \quad (6)$$

It is clear from Eqs. (5) and (6) that  $\chi_b$  and  $\kappa$  are functions of the boundary conditions  $\bar{V}_a$  and  $\bar{A}_a$ , and do not depend on the MILO radii,  $r_a$  and  $r_c$ . While  $\chi_b$  and  $\kappa$  do not have immediate physical meanings, the Brillouin flow is completely characterized by them<sup>23</sup>.

The anode current,  $I_a$ , which is the total input current, is equal to the sum of the cathode surface current,  $I_c$ , and the electron current carried within the Brillouin hub,  $I_e$  (Fig. 1). They are given by (all  $I$ 's are positive by convention)<sup>23</sup>

$$I_e = I_a - I_c = I_c(I_a/I_c - 1) \quad (7)$$

$$I_c = \left( \frac{8.53 \text{ kA}}{\ln(r_a/r_c)} \right) \kappa \quad (8a)$$

$$I_a = \left( \frac{8.53 \text{ kA}}{\ln(r_a/r_c)} \right) \kappa \cosh \chi_b \quad (8b)$$

$$I_a : I_c : I_e = \cosh \chi_b : 1 : [\cosh \chi_b - 1] \quad (9)$$

The targeted operating point of the MELBA MILO experiment is  $V_a \approx 250$  kV and  $I_a \approx 10$  kA, to match the parameters of the MELBA facility. By virtue of Eqs. (5), (6), and (8), the aspect ratio  $r_a/r_c$  is the key parameter in achieving magnetic insulation at this relatively-low input current by operating at high impedance (compared to other MILO devices), which has been suggested previously<sup>7,28,29</sup>. However, Eq. (9) states the relative portion of current carried within the Brillouin flow is not a function of the aspect ratio. After some parameterization, the cathode ( $r_c$ ) and anode radii ( $r_a$ ) were set to 7 mm and 25 mm, respectively (aspect ratio of 3.6). With  $r_c$  and  $r_a$  defined, the currents  $I_a$ ,  $I_e$ ,  $I_c$ , and the ratio  $I_e/I_a$  may be calculated explicitly from Eqs. (8) and (9), and are shown in Fig. 2, plotted as a function of the flux ratio  $f = A_a/A_a^{min}$ .

The input current  $I_a$ , plotted in Fig. 2a, displays a peculiar feature. For fixed voltage, as the degree of magnetic insulation  $f = A_a/A_a^{min}$  decreases towards unity (i.e. Hull cutoff),  $I_a$  exhibits a *v-shaped curve*<sup>23</sup>. The v-shaped region,  $1 < A_a/A_a^{min} < f_u$ , is marked by the horizontal pink line in Fig. 2a for the  $V_a = 275$  kV case. The minimum value of  $I_a$  is  $I_a^{min}$  (see Eq. 11), occurring at  $f = f_m$  (slightly greater than unity). The Hull cutoff current,  $I_a^{HC}$  (at  $f = 1$  and at  $f = f_u$ ), is the maximum current in the v-shaped region (see Eq. 10 below). Within the v-shaped curve, one value of  $I_a$  may yield two possible values of  $A_a/A_a^{min}$ . *This double-valued feature means that the input current necessary to insulate the diode could be less than the input current required to achieve Hull cutoff (where  $f = 1$ )*<sup>23</sup>. Fig. 3a shows  $f_m$  and  $f_u$  as a function of  $V_a$ . Where the diode is insulated beyond the minimum current,  $f > f_m$ , the input current increases monotonically with the flux ratio. A similar v-shaped relation between the electron hub current and the externally imposed magnetic flux was reported previously<sup>30,31</sup>.

The existence of the v-shaped curve is made apparent when considering Fig. 2b, Fig. 2c, and Eq. (7). The input current  $I_a$  is simply the sum of the current carried on the cathode surface  $I_c$  and the current within the Brillouin hub  $I_e$ . Fig. 2b demonstrates that while  $I_e$  decreases monotonically, its slope is infinitely steep at Hull cutoff<sup>23</sup>. Meanwhile, it is clear from Fig. 2c that the cathode current is a gradually increasing function of the flux ratio. The drastic increase in  $I_e$  as magnetic insulation is lost results in the v-shaped region in  $I_a$  as shown in Fig. 2a.

Fig. 2d gives the ratio  $I_e/I_a$ , which quantitatively measures the fraction of magnetic insulation provided only by the electron flow within the Brillouin hub. At sufficiently large flux ratio (i.e.  $f > 1.3$ ), the electron hub current accounts for less than 15% of the total current (and thus less than 15% of magnetic insulation) at voltages up to 500 kV.

The current at the Hull cutoff condition  $I_a^{HC}$ , and the minimum current  $I_a^{min}$ , are expressed in Eqs. (10) and (11), respectively. The solution to Eq. (10) is analytic by setting  $A_a = A_a^{min}$  (Appendix A of Ref. 23), whereas Eq. (11) must be obtained numerically, as given in Fig. 3b,

$$I_a^{HC} = \left( \frac{8.53 \text{ kA}}{\ln(r_a/r_c)} \right) \gamma_a \cosh^{-1}(\gamma_a) \quad (10)$$

$$I_a^{min} = \left( \frac{8.53 \text{ kA}}{\ln(r_a/r_c)} \right) \times \min[\kappa \cosh \chi_b] \quad (11)$$

where, for a given voltage,  $\min[\kappa \cosh \chi_b]$  is the value of  $\kappa \cosh \chi_b$  shown in Fig. 3b corresponding to  $I_a^{min}$  ( $f = f_m$ ). In conjunction with the MILO radii  $r_a$  and  $r_c$ , the red and black curves in Fig. 3b may be used to compute  $I_a^{HC}$  and  $I_a^{min}$  by virtue of Eqs. (10) and (11), respectively. In Fig. 3a,  $f_u$  increases monotonically with the voltage, whereas  $f_m$  peaks at  $\sim 1.1$ . Thus, the domain of the v-shaped curve expands in flux ratio as the voltage increases. At  $V_a \approx 500$  kV, a common MILO operating voltage,  $f_u \approx 1.5$ . Also note that  $\min[\kappa \cosh \chi_b]$  is the same as the minimum value of the v-shaped curve in Fig. 8(a) of Ref. 23.

As previously mentioned,  $\chi_b$  and  $\kappa$  completely characterize the electron flow characteristics (after the geometry has been specified). Parameters such as the normalized Brillouin flow speed at the edge of the Brillouin hub, and its location,  $r = r_b$ , are given by<sup>23</sup>,

$$\beta_b = \frac{\gamma_a \bar{A}_a - \sqrt{\bar{A}_a^2 - (\bar{A}_a^{min})^2}}{\bar{A}_a^2 + 1} = \tanh(\chi_b) \quad (12)$$

$$\gamma_b = 1/\sqrt{1 - \beta_b^2} = \cosh(\chi_b) \quad (13)$$

$$r_b = r_c e^{\chi_b/\bar{\kappa}} \quad (14)$$

where  $\bar{\kappa} = \kappa/\ln(r_a/r_c)$ , and the subscript “b” is used to denote values evaluated at the outer edge of the Brillouin hub,  $r_b$ . In the Brillouin flow model, the Buneman-Hartree condition (BH) reads,  $\beta_{ph} = \beta_b$ , or<sup>23</sup>,

$$\bar{V}_a = \bar{A}_a \beta_{ph} - [1 - \sqrt{1 - \beta_{ph}^2}] \quad (15)$$

where  $\beta_{ph}$  is the normalized phase velocity of the circuit wave, set equal to the electron axial velocity evaluated at the top of the Brillouin hub  $\beta_b$ .

The radial thickness of the electron hub ( $r_b - r_c$ ) normalized to the AK gap distance ( $r_a - r_c$ ) may be calculated using Eq. (14) and is plotted in Fig. 4a. Despite the counter-intuitive left-side branch of the v-shaped curve in Fig. 2a ( $f < f_m$ ), the hub thickness decreases monotonically for  $f > 1$ . At  $\sim 250$  kV,  $f_m \approx 1.05$  (Fig. 3a), where the hub occupies *half* of the AK gap (Fig. 4a). This illustrates that, as magnetic insulation is lost, the edge of the Brillouin hub rapidly approaches the anode, at the same time dramatically increasing  $I_e$  (Fig. 2b). Conversely, Fig. 4a shows it is not necessary to achieve insulation far above Hull cutoff to constrain the edge of the hub within  $\sim 20\%$  of the AK gap distance ( $f \approx 1.3$ ).

In a similar fashion to the hub radius, the beam velocity at the edge of the Brillouin hub  $\beta_b$ , obtained via Eq. (12) and shown in Fig. 4b, decreases quickly after magnetic insulation is achieved. The MILO presented in this work was designed with an RF phase velocity of  $\sim 0.3c$ . Fig. 4b shows that at

This is the author's peer reviewed, accepted manuscript. However, the online version of record will be different from this version once it has been copyedited and typeset.

PLEASE CITE THIS ARTICLE AS DOI: 10.1063/1.50071455

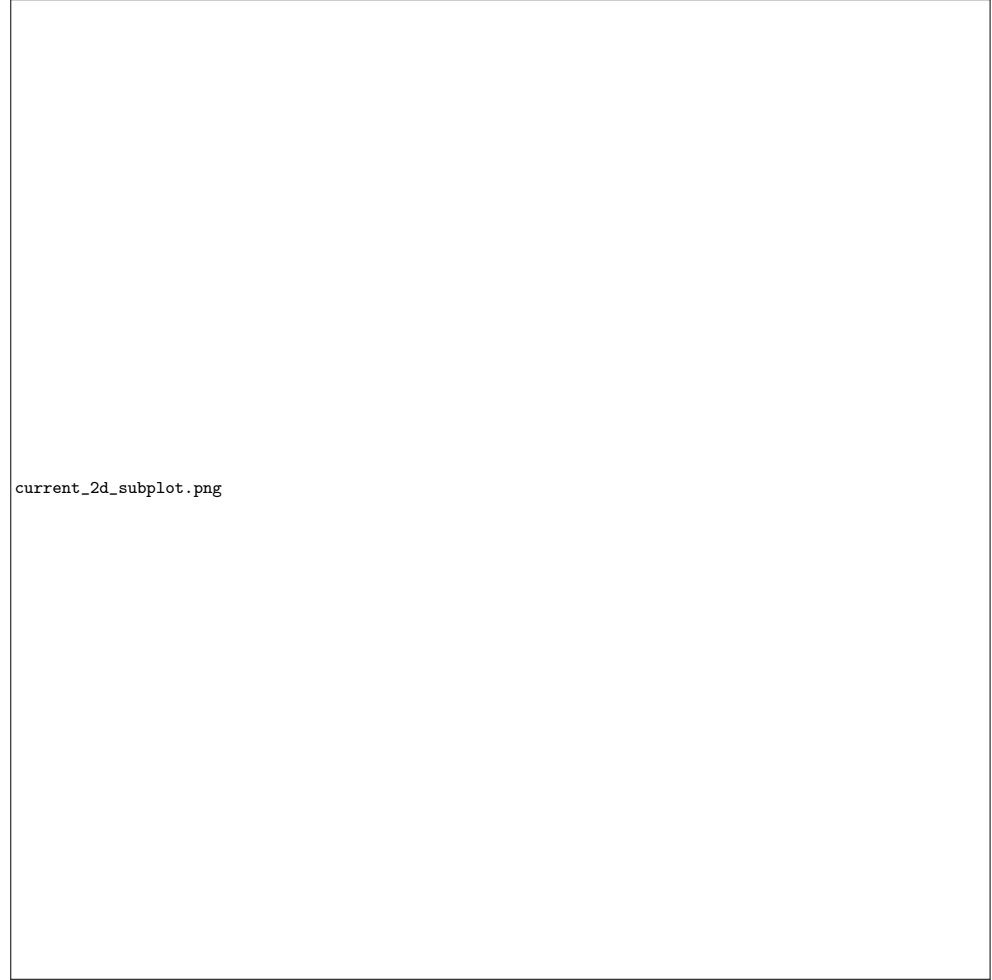


FIG. 2. Input current  $I_a$  (a), electron hub current  $I_e$  (b), cathode surface current  $I_c$  (c), and  $I_e/I_a$  (d) as a function of flux ratio  $f = A_a/A_a^{min}$  and parameterized over voltage  $V_a$ , as determined from Eqs. (8) and (9). The Hull cutoff condition is satisfied for  $f > 1$ . As  $f$  decreases towards unity, a v-shaped region appears in  $I_a$  due to the large increase in  $I_e$  in this parameter space. The maximum current of the v-shaped regime is the Hull cutoff current,  $I_a^{HC}$ , which is observed at  $f = 1$  and at  $f = f_u$  (the right vertical line). The minimum current of the v-shaped curve is  $I_a^{min}$ , at  $f = f_m$  (the left vertical line). (a-c) are relevant to the specific geometry applied to experiments presented in this work, while (d) is general.

$\sim 250$  kV,  $\beta_b < 0.3$  near  $f > 1.5$ ; thus, for the SWS to synchronize with some electrons within the Brillouin flow, operation is expected in the range  $1 < f < 1.5$ . Fig. 4b and Eq. (12) apply to MILOs generally, because  $\beta_b$  is independent of the MILO radii  $r_a$  and  $r_c$ .

Finally, the theoretical maximum efficiency of MILO is estimated to be,

$$\eta = \frac{I_e(V_a - \Delta\phi_b)}{I_a V_a} = (1 - \gamma_b^{-1})(1 - \Delta\phi_b/V_a) \quad (16)$$

where  $\Delta\phi_b = (\gamma_b - 1)mc^2/e$  is the potential drop from the edge of the Brillouin hub to the edge of the cathode, representing the electron kinetic energy. Thus, the difference  $(V_a - \Delta\phi_b)$

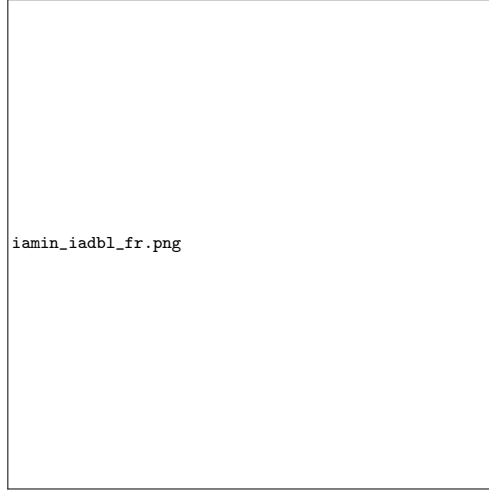


FIG. 3. (a) Flux ratio  $f_m$  at  $I_a^{min}$  (black, dashed) and  $f_u$  at  $I_a^{HC}$  (red) as a function of voltage. The v-shaped curve is double-valued in the range  $1 < f < f_u$ . (b) The crucial factor in Eq. (8b) for the anode current,  $\kappa \cosh(\chi_b)$ , at  $f = 1$  (red) and at  $f_m$  (black, dashed). The curves in (a) and (b) apply to any cylindrical MILO geometry. They are independent of the MILO radii,  $r_a$  and  $r_c$ .



FIG. 4. Normalized hub width (a), normalized Brillouin hub edge velocity (b), and maximum total efficiency (c) as a function of the flux ratio  $f = A_a/A_a^{min}$  and parameterized over voltage  $V_a$ , as determined from Eqs. (14), (12), and (16), respectively. The traces in (a) overlap because the hub radius is a weak function of voltage. (b) and (c) apply to MILOs generally.

is the remaining potential energy available for conversion to RF. This expression assumes that all electrons in the Brillouin hub become spoke electrons and convert all their potential energy to RF; the kinetic energy thus enables synchronism, but is not absorbed by the RF wave. Equation (16), plotted in Fig. 4c, is essentially the same expression given elsewhere for magnetron efficiency<sup>32</sup>, but another term  $I_e/I_a = (1 - \gamma_b^{-1})$  appears, significantly reducing the efficiency. The potential energy drop experienced by the spoke electrons vanishes to zero at Hull cutoff ( $f = 1$ ), at which point the Brillouin hub touches the anode. The efficiency decreases as the diode becomes insulated beyond the local maximum ( $f \approx 1.06$ ) because  $I_a$  must increase to raise the magnetic field while  $I_e$  decreases (Fig. 2a and Fig. 2b). As a result, it is advantageous to operate the MILO at higher voltage and close to Hull Cutoff, but not so close that the potential energy goes to zero. These considerations are consistent with the experience that MILOs have low efficiency compared to magnetrons. This effect could potentially be partially ameliorated by applying some portion of the magnetic field by another means, such as weak permanent magnets in a magnetron-MILO hybrid configuration<sup>23,33</sup>.

### III. SIMULATION

After using the theory to determine the cathode radius and vane inner radius (7 mm and 25 mm, respectively), the SWS cavity dimensions were produced using HFSS<sup>34</sup>. The outer radius of the 5-cavity resonant SWS was set to 11.2 cm, placing the  $TM_{01}$   $\pi$ -mode cold frequency at 1.041 GHz. The circuit periodicity (pitch) is 4.3 cm, resulting in an RF phase velocity of  $0.3c$ . The vane width is 1.075 cm, one quarter of the pitch. The inner radius of the final vane is 3.75 cm. Two choke cavities are placed upstream of the 5-cavity SWS. The outer radius and pitch of the two choke cavities are 13 cm and 3.225 cm, respectively, such that the desired  $TM_{01}$   $\pi$ -mode of the resonant cavities would be evanescent in the choke.

Three-dimensional particle-in-cell simulations were performed in CST-Particle Studio<sup>35</sup> and ICEPIC<sup>36</sup> to produce a feasible source design and validate their predictions against experiment. These models were nearly identical; voltage monitors were placed across each cavity, electrons were emitted from the cathode via explosive emission, and wave absorbing boundaries were placed at the voltage input and microwave output. Voltage and current monitors were placed at the input and output to measure the injected power and output power. An additional current monitor was placed between the final vane and the beam collector to measure the downstream current. The ICEPIC models were performed with a fixed-resolution of 1 mm, whereas the CST-PS models implemented a variable mesh. Voltage was injected at the input with a linear 200 ns risetime, rising to a 200 ns flat-top of  $V_a \approx -230$  kV applied to the cathode (the anode was held at ground potential, 0 V). The radius of the downstream cathode,  $r_d$  (see Fig. 5b), was parameterized as an independent variable. Manipulation of  $r_d$  affects the downstream current, thus altering the magnetic field upstream in the cavity region in a manner similar to varying the magnetic field of a magnetron.

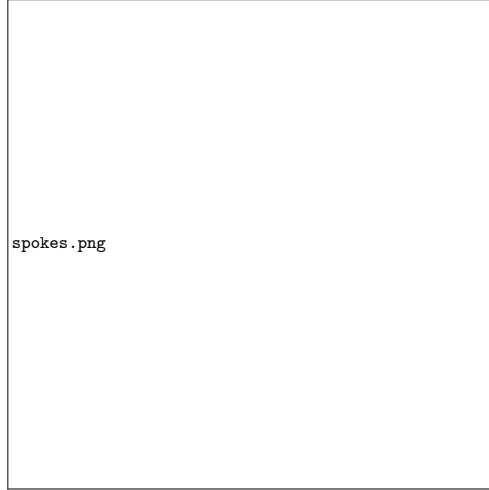


FIG. 5. PIC simulations of the MILO in (a) ICEPIC and (b) CST-PS. Cavities are labeled in sequential order. Electrons are emitted from the purple highlighted portions of the cathode in (b) via the explosive emission model. The current collected in the downstream diode establishes the crossed-field flow in the cavity region for interaction between the electron hub and the electromagnetic wave. This downstream current is manipulated by varying  $r_d$  as an independent variable.

Both models predict  $\pi$ -mode operation across a similar range of  $r_d$ . Azimuthally symmetric electron spoke generation in every-other cavity is illustrated in Fig. 5. The choke cavities were not excited into resonance in any of the simulations. No mode competition was observed with higher-order modes or other modes of the fundamental bandpass of the 5-cavity structure.

It is well known that  $\pi$ -mode operation can be maintained across a wide range of driving voltages for a fixed MILO impedance, as the ExB drift velocity (scaling as E/B) is relatively insensitive to such variation. This is because the current (and thus B field) increases as the driving voltage (and thus E field) is increased; as a result, the ratio E/B remains relatively constant. However, the simulations show that by varying the diode impedance of the MILO (by varying  $r_d$ ), the fraction of current flowing across the AK gap in the SWS, versus that which crosses the AK gap in the diode region downstream of the SWS, can be controlled. As demonstrated in Fig. 6, this control results in a relatively wide operating space at the drive voltage of  $\sim 230$  kV.

Additionally, Fig. 6 shows the simulated total current ( $I_a$ ), measured at the input, does not vary with  $r_d$  over the range where microwaves are generated ( $r_d = 7$ -14 mm), and is less than the current at the Hull cutoff condition ( $I_a^{HC}$ ) (see the horizontal blue dashed line in Fig. 6). At the same time,  $I_d$  (current drawn in the downstream diode) increases with  $r_d$  in this range, whereas  $I_{SWS}$  (current collected on the SWS vanes)

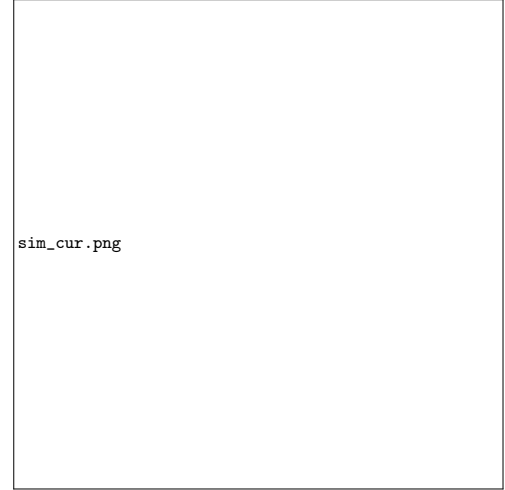


FIG. 6. Current as a function of  $r_d$ . The total current  $I_a$  is measured at the input, while the downstream diode current  $I_d$  and SWS current  $I_{SWS}$  represent the current collected on the beam dump and SWS vanes, respectively. From  $r_d = 8$  - 13 mm, the total current is constant at  $\sim 8.5$  kA. However,  $I_d$  increases with  $r_d$ , resulting in an equivalent decrease in  $I_{SWS}$ . The plotted values are from when the simulations reached a steady state, at a flat-top voltage of  $V_a \approx -230$  kV.

decreases an equal amount, resulting in a net zero change in  $I_a$ . This suggests a maximum current that can be injected, with a tradeoff between the current available to the SWS and the downstream current. For  $r_d > 14$  mm, the downstream current exceeds the Hull cutoff current and the SWS current drops to zero, resulting in a cessation of microwave generation (Fig. 7a).

Considering the specific simulation from ICEPIC at  $r_d = 12$  mm ( $V_a = 239$  kV,  $I_a = 8.57$  kA) and comparing with  $I_a$  at  $V_a = 235$  kV (Fig. 2a), the simulated input current intersects the v-shaped curve at  $f \approx 1.004$  and  $f \approx 1.14$ . Going a step further, the assumption that  $I_d = I_c$  and  $I_{SWS} = I_e$  can be made. Strictly speaking,  $I_d \neq I_c$  and  $I_{SWS} \neq I_e$  because there is some fraction of the Brillouin hub that does not strike the vanes, and instead propagates toward the downstream diode where it is eventually collected. However,  $I_d$  and  $I_{SWS}$  may serve as useful approximations of  $I_c$  and  $I_e$ , respectively; this is further discussed in the appendix. Assuming  $I_d$  (6.58 kA) =  $I_c$ , the corresponding flux ratio is  $f \approx 1.04$  (Fig. 2c). Similarly for the SWS current, the flux ratio estimate is  $f \approx 1.013$  (assuming  $I_{SWS} = 1.99$  kA =  $I_e$  from Fig. 2b). All of these flux ratio estimates from the simulation lie within the v-shaped curve, where the Hull cutoff condition has been achieved ( $f > 1$ ) and  $I_a^{min} < I_a < I_a^{HC}$ , extending from  $1 < f < 1.25$  at 235 kV. It is clear that the simulations predict operation much closer to the Hull cutoff condition than the Buneman-Hartree condition, which occurs at  $f = 1.56$  at 235 kV and a phase velocity

TABLE I. MILO metrics compiled in CST-PS and ICEPIC for two different values of  $r_d$ . In CST, all simulations were performed at -230 kV. In ICEPIC, the  $r_d = 10$  mm simulation was performed at 240 kV, and  $r_d = 12$  mm at 239 kV. In calculating the percent difference, the ICEPIC value was used in the denominator.

Metric	$r_d = 10$ mm			$r_d = 12$ mm		
	CST	ICEPIC	% Difference	CST	ICEPIC	% Difference
Output Power (MW)	68	76	10.5	72	69	4.3
Current $I_a$ (kA)	8.6	8.5	1.2	8.6	8.6	0
Impedance ( $\Omega$ )	26.7	28.1	5	26.7	27.8	4
Frequency (GHz)	1.008	1.032	2.3	1.012	1.034	2.1
Total Efficiency (%)	3.4	3.7	8.1	3.6	3.4	5.9
Electronic Efficiency (%)	12.1	11.6	4.3	21.3	14.5	46.9

of  $0.3c$  according to Eq. (15).

These PIC simulations estimate microwave generation of  $\sim 70$ -80 MW at  $\sim 1$  GHz with  $r_d \approx 10$ -12 mm, shown in Fig. 7a. The operating frequency corresponds to the  $\pi$ -mode (cold frequency of 1.041 GHz) shifted downward 10-30 MHz, depending on the code. The downward shift is most likely due to beam loading<sup>37</sup>. As  $r_d$  increased and  $I_{SWS}$  decreased, the output frequency increased, indicating the effect of beam loading had diminished. The  $4\pi/5$ -mode cold frequency is 1.009 GHz, but this mode is not considered dominant after reviewing the field patterns, cavity RMS voltages, and spoke formation in the device during operation. The  $\sim 20$  MHz difference between CST-PS and ICEPIC is possibly because the ICEPIC models utilized a mesh with cubic 1 mm resolution, whereas CST-PS used a variable mesh to conform to the device's physical features. Differences between geometric fidelity due to the variable mesh (CST-PS) balanced against formal second order accuracy with the uniform mesh (ICEPIC) might explain some of the discrepancy<sup>38</sup>. Additional sources of inconsistency may be due to differences in the wave absorbing boundaries between the codes, where the default settings were used and good absorption of the outgoing waves was confirmed, but ultimately the boundaries were not made identical<sup>39</sup>.

The total efficiency of a MILO, defined as the ratio of microwave output power over the input electromagnetic power (product of input voltage and current), is commonly in the range of 4-6%<sup>8-11</sup>, although higher efficiencies ( $> 10\%$ ) have been achieved<sup>40,41</sup>. Meanwhile, the electronic efficiency of a MILO is defined here as the ratio of output microwave power to the energy transfer rate on the anode vanes (product of input voltage and current collected on SWS), similar to the cited definition for magnetrons<sup>42</sup>. Fig. 7b gives both quantities as a function of  $r_d$ , showing adequate performance for efficiency. By optimizing  $r_d$ , simulations estimate the device can reach  $\sim 3.5\%$  total efficiency and  $\sim 20\%$  electronic efficiency. Both of these metrics could potentially be improved by tapering the inner radius of multiple vanes closest to the extractor<sup>15</sup>, implementing a focusing electrode on the cathode<sup>43</sup>, or machining ridge structures into the vanes<sup>19,44</sup>.

Several quantities of interest are tabulated in Table I for  $r_d = 10$  mm and 12 mm, comparing the estimates from CST-PS and ICEPIC. The codes agreed reasonably well overall, with differences less than 10% for most of these key parameters. However, it was difficult to improve agreement even with in-

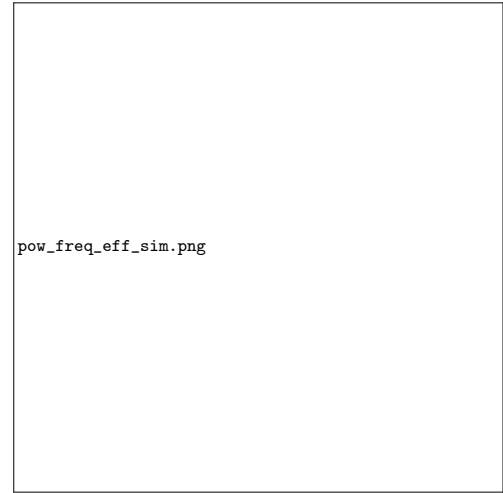


FIG. 7. Microwave output power and dominant frequency (a) and total efficiency and electronic efficiency (b) over  $r_d$ . With  $r_d \approx 10$ -12 mm, both codes predict microwave generation of approximately 70-80 MW in the  $\pi$ -mode at  $\sim 1$  GHz.

creased mesh refinement in CST-PS, and in some cases, the agreement deteriorated with increased mesh refinement. A convergence study was not performed in ICEPIC, but 1 mm resolution has been recommended for devices near this frequency previously<sup>45</sup>. In general, higher confidence is placed in the ICEPIC results because the variations in parameters such as the output power and current were smoother than CST-PS as  $r_d$  was iterated.

#### IV. EXPERIMENTAL CONFIGURATION

The primary components of the MILO include a central cathode, a series of resonant cavities, and a microwave extractor that doubles as a beam collector. These are all represented in Fig. 8. The cathode rod is covered with a velvet-cloth emitter in the cavity region, where the cathode radius ( $r_c$ ) is 7 mm.

This is the author's peer reviewed, accepted manuscript. However, the online version of record will be different from this version once it has been copyedited and typeset.

PLEASE CITE THIS ARTICLE AS DOI: 10.1063/5.0071455

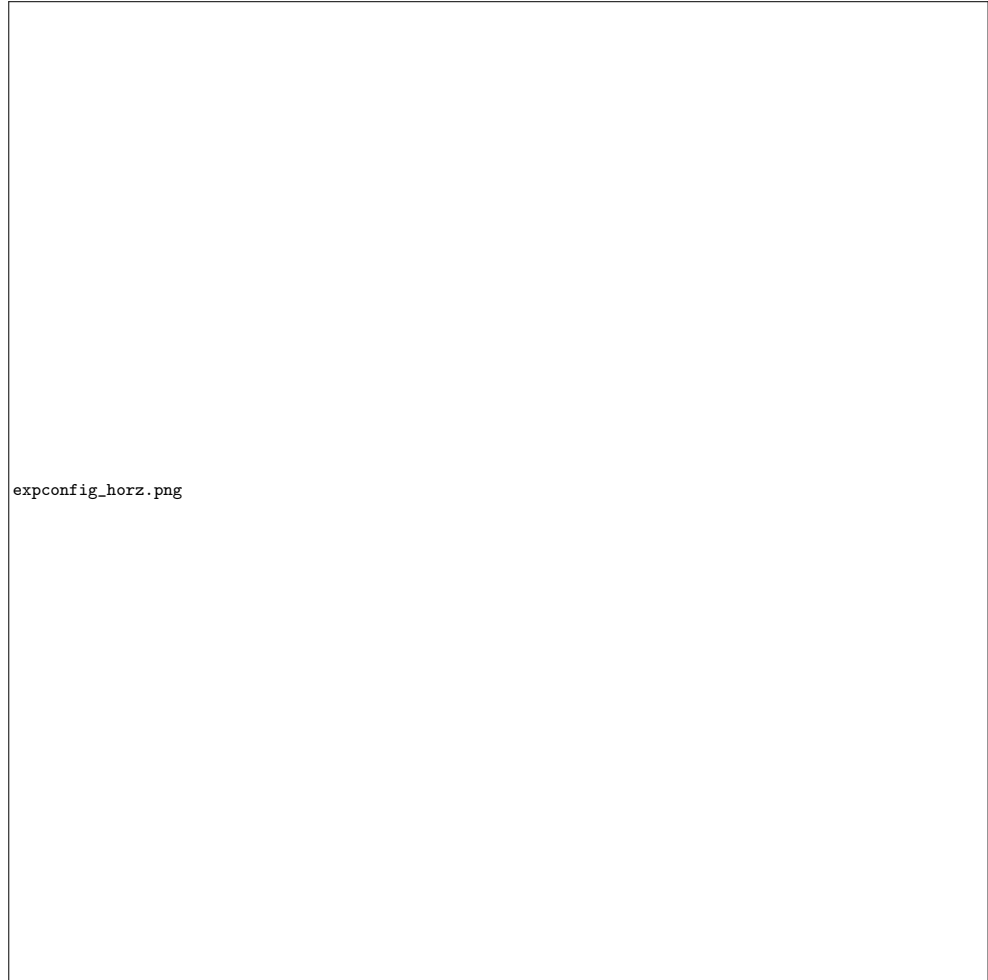


FIG. 8. Experimental configuration of the MILO. Emission is allowed from the cathode in two areas. The first is in the cavity region, where the cathode is of radius  $r_c = 7$  mm. The second emitter is on the downstream cathode, of radius  $r_d$ , which is used as an independent variable to manipulate the current drawn in the downstream diode.

At the end of the cathode, there is an additional velvet emitter on the downstream cathode whose radius ( $r_d$ ) is an independent variable near 10 mm. The velvet emitters were placed in the same regions as implemented in the PIC simulations (see Fig. 5). The purpose of varying the downstream cathode is to manipulate the current drawn to the beam collector, thus altering the azimuthal magnetic field upstream in the cavity region. The beam collector is made of fine-grained graphite, which sublimates into dust when struck by the high-energy beam. The collector is grounded through the quarter-wave

shorts and distributed field adaptor (DFA) that converts coaxial waveguide to rectangular waveguide.

The slow wave structure (SWS) consists of two choke cavities and five resonant cavities, the latter which define the operating frequency ( $\sim 1$  GHz). The choke cavities are evanescent to the desired  $TM_{01}$   $\pi$ -mode of the resonant cavities, which enforces propagation of the RF wave towards the output waveguide. The desired  $TM_{01}$   $\pi$ -mode excites the output coaxial transmission line in a TEM wave. Three quarter-wave shorting stubs, placed with azimuthal symmetry, provide



TABLE II. Experimental average metrics of the MILO on MELBA. Average performance was significantly improved for  $r_d = 10$  mm, but was still highly variable in both experiments. The output power, voltage, current, impedance, and efficiency were all taken at the instant of peak microwave output power.

Metric	$r_d = 8$ mm	$r_d = 10$ mm
Frequency (GHz)	$980 \pm 22$	$993 \pm 22$
Output Power (MW)	$1.4 \pm 1.4$	$10 \pm 7$
Voltage (kV)	$259 \pm 25$	$243 \pm 21$
Current $I_a$ (kA)	$9.3 \pm 0.8$	$9 \pm 0.7$
Impedance ( $\Omega$ )	$28 \pm 1.5$	$27 \pm 1.6$
Efficiency (%)	$0.06 \pm 0.06$	$0.49 \pm 0.36$
Energy (J)	$0.089 \pm 0.05$	$0.64 \pm 0.44$
Pulse Length (ns)	$121 \pm 68$	$118 \pm 43$
Startup Time (ns)	$287 \pm 71$	$251 \pm 53$

physical support to the coaxial center conductor and are transparent to the RF wave. The coaxial line is then adapted to a smaller cross section through a tapered section, and converts to WR-650 waveguide at the DFA. From 0.94 GHz to 1.02 GHz, the DFA transmission ( $S_{21}$ ) ranges between -0.2 dB to -0.02 dB<sup>46</sup>. At the end of the waveguide, an ECCOSORB microwave terminator absorbs the RF wave with minimum return loss of 9 dB (at 993 MHz). This microwave extraction scheme contrasts with other methods implemented on MILOs, which often radiate out of the end, such as through a belljar<sup>47</sup>. The microwave signal is sampled in the waveguide using a loop directional coupler and split into two transmission lines to measure spectral content and power. One path was used to measure spectral content directly with an Agilent 54855A oscilloscope (6 GHz, 20 GSa/s), while the other measured power by rectifying with a calibrated HP 8472B Low-Barrier Schottky Diode (0.3-dB precision) detector before terminating at an oscilloscope.

## V. EXPERIMENTAL RESULTS

Experiments were performed using the Michigan Electron Long Beam Accelerator with Ceramic Insulator (MELBA-C)<sup>20,48</sup> facility at  $\sim 250$  kV and  $\sim 10$  kA. The experiments discussed herein used two different values of downstream cathode radius,  $r_d$  (8 mm, 10 mm) over MELBA shots 18084-18208. This adjustment of  $r_d$  was the only difference between the experiments; the anode and cathode were otherwise left unchanged. Of the 125 shots, 21 were taken at  $r_d = 8$  mm, and 104 at  $r_d = 10$  mm. Nine of these shots (all with  $r_d = 10$  mm) were removed from the data set because either the injected voltage waveform was inadequate (maximum voltage of  $< 200$  kV), or the measurement of voltage or current was corrupted. In Section V A, the general operating characteristics of the device are outlined. In Section V B, these MELBA experiments are compared with the theory discussed in Section II. Finally, Section V C contrasts the MELBA experiment with other MILO experiments and the theory.

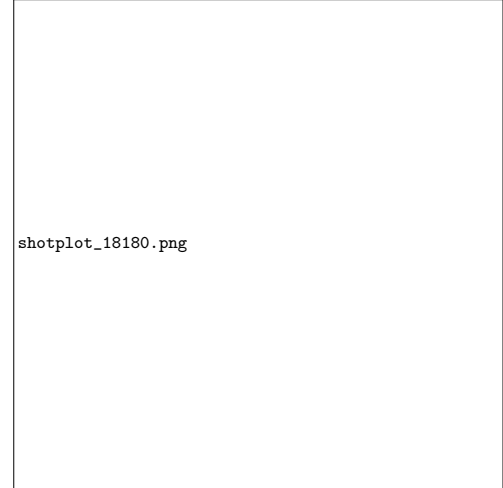


FIG. 9. (a) Voltage, current, impedance, and microwave power overlaid for MELBA shot 18180. Peak microwave generation was 22 MW, at which instant the voltage, current, and impedance were 250 kV, 9.3 kA, and  $27 \Omega$ . (b) Time-frequency analysis of the raw RF trace sampled in the output waveguide for MELBA shot 18180. The dominant frequency was 994 MHz with no significant competing mode.

### A. Device Characteristics

The primary measurements from this experiment were the input voltage, input current, and output microwave power. These are each displayed, along with the impedance, for MELBA shot 18180 in Fig. 9a. Microwave generation reaches a maximum of 22 MW at nearly the same instant at which maximum voltage is observed. At this peak, the voltage and current were 250 kV and 9.3 kA, corresponding to an impedance of  $27 \Omega$  and peak total efficiency of 1% (output microwave power divided by input cathode power at peak microwave generation). In the entire data set, the highest total efficiency and power reached by the device were 1.4% and 26 MW, respectively.

The microwave pulse length and total energy production were 117 ns and 1.4 J, respectively, for shot 18180. Shortly after microwave generation was quenched, likely by plasma gap closure in the cavity region<sup>49</sup>, the voltage began to fall. Total impedance collapse is observed as the current ramped to a peak 23 kA and voltage decreased below 50 kV. This was observed on nearly every shot because it was difficult to achieve crowbar conditions with this low impedance device. Time-frequency analysis of Fig. 9b is shown over a 300 MHz band centered at 1 GHz. The dominant frequency was 994 MHz, with no evidence of mode competition throughout the shot.

Overall, the experiments operated at parameters very similar to the estimates from the PIC simulations. A direct com-

parison of Table I and Table II shows that the experimental voltage, current, and impedance, all listed at the instant of peak microwave generation, were accurately predicted by the PIC simulations (which were performed at 230 kV to approximate the experiments). The impedance was the most consistent predictor of MILO operation, and it agrees very well with the PIC estimates of the impedance over the range where microwave generation occurred (Fig. 6,  $r_d = 7\text{-}14$  mm). The frequency estimates were not as accurate, which was discussed in Section III. The output power estimates were off by a large factor, however, and warrant further discussion.

The peak output power from the two experiments was highly inconsistent from shot-to-shot, but improved as  $r_d$  increased from 8 to 10 mm. Fig. 10 shows the results from each shot, with the 10-shot rolling average and 68% confidence interval. Shots that took place to the left of the vertical dashed line were  $r_d = 8$  mm (18084-18104), and all shots to the right were  $r_d = 10$  mm (18105-18208). The  $r_d = 8$  mm experiment was terminated after 21 shots because the output power was consistently less than 5 MW, whereas the  $r_d = 10$  mm experiment displayed significant improvement within the first twenty shots. Toward the end of the  $r_d = 10$  mm experiment, the device demonstrated its optimal performance with the 10-shot rolling average remaining near 15 MW for over 10 shots. Six of the final seven shots did not reach higher than 200 kV, and consequently the microwave generation was poor; because the injected voltage was inadequate for these shots, they are not considered in the calculation of the red traces shown in Fig. 10. Disassembly of the experiment revealed significant damage to the downstream cathode velvet that likely shorted the diode and disabled operation<sup>27</sup>.

The high variance in output power requires more investigation. Implementation of a Rogowski coil between the final vane and the beam dump, similar to that from the simulations, would illuminate the role of current delivered to the downstream diode ( $I_d$ ). This diagnostic would also provide an estimate of the SWS current ( $I_{SWS}$ ), assuming  $I_{SWS} = I_a - I_d$ . Both the highly variant and low-power microwave generation ( $P_{out} < 5$  MW) could be explained by inconsistent  $I_d$  and low  $I_{SWS}$ , respectively. The simulation results of Fig. 6 suggest a tradeoff between  $I_{SWS}$  current and  $I_d$ , so it would be useful to measure this ratio. Note the assumption that all current collected upstream of the beam collector would impact the SWS is consistent with the crucial assumption used to derive the efficiency formula, Eq. (16); namely, all Brillouin hub electrons become spoke electrons, all of which participate in the generation of RF power.

Another observation is the highest output powers achieved in experiment ( $\sim 25$  MW) were approximately a factor of three lower than estimates from simulation ( $\sim 70\text{-}80$  MW). The PIC results predicted optimized power generation at  $r_d \approx 10\text{-}12$  mm, close to where the best experimental results were obtained. However, the experiments may have operated to the left of the relative power maximum in Fig. 7a. Additional experiments at other values of  $r_d$  are required to pinpoint the relative power maximum for the experimental system tested.

It is also possible that trapped modes, specifically in the choke cavities, disrupted operation in the desired mode and

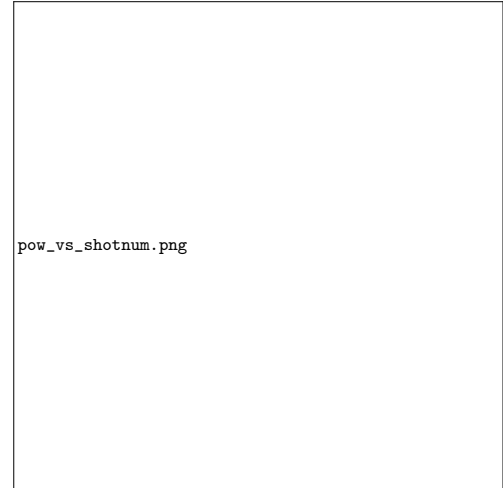


FIG. 10. Peak microwave output power as a function of shot number for the  $r_d = 8$  mm and 10 mm experiments, which occurred to the left and right of the vertical black dashed line, respectively. Individual shots are plotted with black crosses, while the 10-shot rolling average and standard deviation are overlaid in red. Particle-in-cell estimates of the output power were  $\sim 70\text{-}80$  MW.

did not couple out of the device. Competing tones were observed in the output waveguide that likely originated from the choke cavities, and were more prevalent for  $r_d = 8$  mm<sup>27</sup>. This mode competition was considered unlikely because such interactions were not observed in simulations and there are only two choke cavities. Diagnostics such as B-dot loops to measure cavity response<sup>40</sup> would be beneficial, and experiments without the choke section could be worth investigating.

The electrostatic design of the cathode could also be improved. Many MILO experiments maintain the same cathode profile in the downstream diode and cavity regions, or even reduced the cathode radius in the downstream diode<sup>50,51</sup>. One example of an experiment that did increase the cathode radius in the downstream diode<sup>16</sup> demonstrated improved durability to the emitter in the cavity region. However, the difference in radii was not as significant as these experiments on MELBA. There are concerns that the downstream diode may draw more current than expected from the simulations due to the larger-radius downstream cathode, leaving little current to interact with the SWS. However, experimentally, this appears to not be the case because  $r_d = 10$  mm performed much better than  $r_d = 8$  mm. Nonetheless, future designs will consider setting  $r_d = r_c$  to reduce field enhancement in this region. Instead of altering the downstream radius, the axial length of the downstream cathode could be varied experimentally to manipulate the current delivered to the downstream diode. In addition, modifications could be made at the launch point, upstream of the resonant cavities, to improve electron flow in the cavity

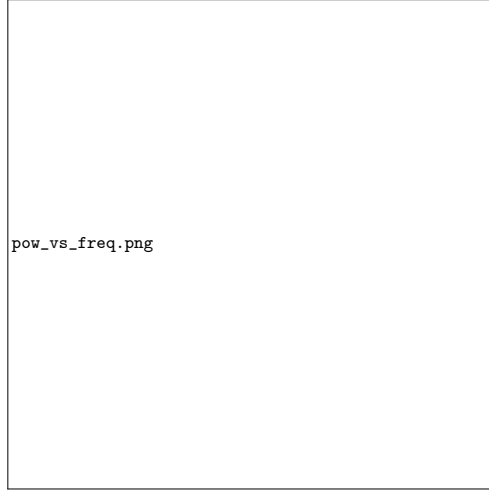


FIG. 11. Power versus frequency for  $r_d = 8$  mm and 10 mm, compared with the CST-PS hot-test estimates of the  $\pi$ -mode and  $4\pi/5$ -mode frequencies. The majority of  $r_d = 8$  mm shots skew toward the expected  $4\pi/5$  frequency, while  $r_d = 10$  mm agrees more with the  $\pi$ -mode frequency.

region<sup>52</sup>.

Microwave output frequency information is displayed in Fig. 11 and compared with hot-test estimates of the  $\pi$ -mode (1.008 GHz, Table I) and  $4\pi/5$ -mode from CST-PS. The  $4\pi/5$ -mode was not observed in the simulations, so it is assumed that its cold frequency (1.009 GHz) would decrease an equal amount due to beam loading as the  $\pi$ -mode (1.041 GHz – 1.008 GHz = 33 MHz). Thus, the hot-test estimate of the  $4\pi/5$ -mode frequency is 0.976 GHz. Both of these modes couple to the output extractor with greater than 9 dB return loss (> 87.5% transmission).

A viable case can be made that either the  $4\pi/5$ -mode or the  $\pi$ -mode was dominant in the experiments. The dominant frequency of nearly all experimental shots falls between the cold-test and hot-test estimates of the  $4\pi/5$ -mode, which would indicate dominance in this mode. Note that the phase velocity of the  $4\pi/5$ -mode is higher than the  $\pi$ -mode by  $\sim 20\%$ , making its synchronous condition rather different from the  $\pi$ -mode.

Alternatively, there is a cluster of shots where  $r_d = 10$  mm that fall near the  $4\pi/5$ -mode estimate along with a majority of the  $r_d = 8$  mm shots, generating at most  $\sim 5$  MW. The higher frequency shots, closer to the  $\pi$ -mode hot-test estimate, tend to have significantly improved output power, suggesting a change in operating mode. Many of these successful shots are closer to the  $\pi$ -mode frequency, so it is concluded  $\pi$ -mode was dominant for  $r_d = 10$  mm, whereas the  $r_d = 8$  mm experiment could have operated primarily in the  $4\pi/5$ -mode. Additional diagnostics for probing the cavities during operation would be useful in determining the characteristics of these op-

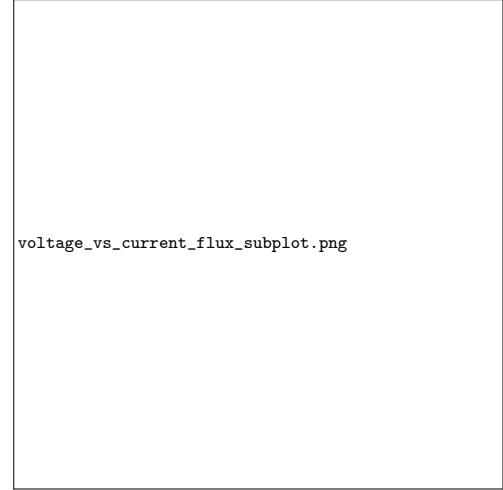


FIG. 12. (a) Voltage and current from each shot at the instant of maximum power generation, overlaid by theory and color bar to represent output power.  $I_a^{min}$  and  $I_a^{HC}$  are the minimum and maximum current in the double-valued range of the v-shaped curve, the latter of which is the current at the Hull cutoff condition. 82% (95/116) of all shots fall within the double-valued region, where  $I_a^{min} < I_a < I_a^{HC}$ . (b) Voltage and normalized flux from theoretical conditions and experimental data points with microwave power output denoted by color bar. With the exception of one shot, all fall within the range between the Hull cutoff and Buneman-Hartree conditions. In (b), it is assumed the MILO was insulated such that  $f > f_m$ .

erating modes.

## B. Comparison with Theory

Section II outlined the theory (Eqs. 7 and 8) used to calculate the total current  $I_a$  as a function of two boundary conditions, the applied voltage  $V_a$  and total magnetic flux  $A_a$  (or equivalently, the flux ratio  $f$ ). By parameterizing  $V_a$  and  $A_a$  (shown in Fig. 2a), it is possible to back out the flux ratio at  $I_a^{min}(f_m)$  and  $I_a^{HC}(f_a)$ , which are shown in Fig. 3a, as well as for individual data points where the voltage and current are measured. Specifically, Eq. (8b) provides the determination of  $f$  in terms of  $V_a$  and  $I_a$ .

Fig. 12a plots the measured voltage and input current for each experimental shot at the instant of maximum power generation, overlaid with traces for  $I_a^{HC}$ ,  $I_a^{min}$ , the BH condition (Eq. 15), and maximum efficiency (which essentially coincides with  $I_a^{min}$ ). Immediately apparent is that many shots fall in the v-shaped curve discussed in depth in Section II, where for a given voltage,  $I_a^{min} < I_a < I_a^{HC}$ . Specifically, 78/95 (82%) of shots for  $r_d = 10$  mm and 17/21 (81%) for  $r_d = 8$  mm are in the v-shaped curve. Of the remaining shots, all operate at currents less than the BH condition with the exception of



FIG. 13. The degree of magnetic insulation at  $I_a^{min}$ ,  $I_a^{HC}$  (respectively equal to  $f_m$ ,  $f_u$ ), and at maximum efficiency, as a function of voltage. These three (3) curves are independent of the anode radius and cathode radius of the MILO. Also shown is the BH condition with phase velocity 0.286c, and experimental data points overlaid. Operation was commonly observed near Hull cutoff.

one low-power shot ( $P_{out} < 5$  MW). All of the highest power shots ( $P_{out} > 20$  MW) fall within the v-shaped curve, which is not surprising given the increased fraction of current in the electron hub closer to Hull cutoff (Fig. 2d). Some moderate-power shots ( $10 \text{ MW} < P_{out} < 20 \text{ MW}$ ) were insulated beyond the double-valued domain, where  $I_a > I_a^{HC}$  ( $f > f_u$ ). Notably, not a single shot occurred at  $I_a < I_a^{min}$  for its specific voltage.

The total current and voltage in experiments can be related directly to the flux ratio  $f$  from the theory through Eq. (8b), yielding the experimental degree of magnetic insulation. The experimental values of voltage and current at the instant of maximum power generation were mapped onto traces similar to those from Fig. 2a, evaluated at the exact experimental voltage, with the assumption that all data points fall on the right-hand side of the v-shaped curve ( $f > f_m$ ). This choice was made to yield a unique relationship between  $V_a$ ,  $I_a$ , and  $f$ . The results are plotted in Fig. 12b, which is similar to the typical BH diagram applied to magnetrons<sup>5-7,25,53</sup>. The primary difference is the known magnetron magnetic field is typically plotted on the horizontal axis, whereas in Fig. 12b the horizontal axis is the total magnetic flux calculated from experimental measurements in tandem with theory. No shots appear between  $1 < f < f_m$  because of the assumption  $f > f_m$ .

It is possible that some shots operated on the left-hand side of the v-shaped curve ( $1 < f < f_m$ ), instead of the right-hand side  $f_m < f < f_u$ . As previously mentioned, a diagnostic to measure  $I_d$  (Fig. 6) could provide an estimate of the monotonic cathode current  $I_c$  (by virtue of Fig. 2c), thereby deter-



FIG. 14. Expected impedance ( $V_a/I_a$  from Fig. 2a) from theory overlaid with experimental impedance at the instant of maximum microwave power generation, against flux ratio with voltage as color bar. Impedance appears to be a consistent predictor of the instant at which the MILO would operate (Table II).

mining whether  $f > f_m$  or  $f < f_m$  in Fig. 2a. This would likely be an overestimate of  $I_c$ , because any hub electrons not collected on the SWS would be picked up in the measurement.

The information displayed in Fig. 12b may be replotted using Eqs. (1)-(4) with the voltage as the horizontal axis and the degree of magnetic insulation as the vertical axis. All the features in Fig. 12 remain, but Fig. 13 indicates the flux ratio is close to unity for nearly every shot: 92% (87/95) and 86% (18/21) of shots were in the range  $1 < f < 1.3$  for  $r_d = 10$  mm and  $r_d = 8$  mm, respectively. On average, the flux ratio was  $1.2 \pm 0.08$  for both  $r_d = 10$  mm and 8 mm; these may be overestimates because of the assumption  $f > f_m$ . Fig. 13 demonstrates clearly that operation near the Hull cutoff condition, specifically within the v-shaped curve, was very consistent. In comparison, the BH condition appears to be significantly less important, which is where magnetrons commonly operate<sup>5-7</sup>. Notably, the flux ratio range between  $I_a^{HC}$  and  $I_a^{min}$  increases with voltage.

Fig. 14 compares the experimental impedance with theoretical expectations, which can be mapped to an experimental flux ratio in the same process described for Fig. 12 and Fig. 13. It is evident that the impedance was often in the v-shaped domain when the MILO was operating. Fig. 14 also suggests a relatively narrow range in the impedance for MILO operation. In this regard, note that the voltage (V) is directly related to the electric field (E) whereas the current (I) is directly related to the magnetic field (B). It follows that the diode impedance (V/I) is directly related to the drift velocity (E/B), which must have the correct value for synchronous interaction to occur

## Physics of Plasmas

(i.e., for RF to be generated). Such a connection remains to be further studied.

### C. Comparison with Other Devices

Finally, a comparison of MILO operation between the experiments presented in previous sections and other devices is given in Table III and Fig. 15. A direct comparison is made possible through the mapping process discussed in Section V B to acquire the experimental flux ratio, and equivalently the normalized flux, which were detailed for the MELBA experiments in Fig. 12b and Fig. 13. Such a comparison between only voltage and current (i.e. Fig. 12a) is insufficient, because each device operates at varying currents influenced by the operating voltage and geometrical aspect ratio (see Eq. 8b). The device parameters required to perform the theoretical calculations are listed in Table III.

The experimental operating voltage is plotted against the normalized flux and flux ratio in Fig. 15a and Fig. 15b, respectively. The BH conditions are plotted separately because they are unique to each experiment, due to its dependence on the phase velocity (Eq. 15). The Hull cutoff condition (Eq. 3) as well as flux ratios,  $f_m$  and  $f_u$ , are independent of the MILO radii  $r_a$  and  $r_c$ .

A common trait between all experiments is they operated at a degree of magnetic insulation less than the BH condition. Additionally, apart from Cousin et al.<sup>16,54</sup>, the experiments operated at  $I_a > I_a^{min}$ , indicating that they achieved magnetic insulation ( $f > 1$ ). In Ref. 16, the voltage and current were 400 kV and 30 kA, at which voltage  $I_a^{min} = 31.75$  kA, suggesting this experiment may have oscillated without achieving magnetic insulation. In this case,  $A_u < A_u^{min}$ , and the experimental operating point would be to the left of the black dashed line in Fig. 15a. Because the theory cannot account for such operating conditions (i.e.,  $A_u$  could not be mapped), this data point was placed at  $f_m$ .

The MELBA experiments, and experiments by Fan<sup>10</sup> and Eastwood<sup>15</sup>, were all mapped into the v-shaped curve ( $1 < f < f_u$ ). Again, it was assumed  $f > f_m$  for these experiments. In the absence of additional experimental evidence, this assumption seems plausible given  $f_m = 1.1$  and  $f_u = 1.5$  at 500 kV. Experiments by Haworth, et al.<sup>9</sup> operated at  $f > f_u$ , magnetically insulated beyond the v-shaped curve (but still less than the BH condition). The experiments by Fan et al. took place at a comparatively high phase velocity, such that the BH condition was in the v-shaped curve.

## VI. CONCLUSION

A new, general theory<sup>23</sup> applied to magnetically insulated coaxial transmission lines was used to design a MILO experiment for operation on MELBA at moderate current ( $\sim 10$  kA) and voltage ( $\sim 250$  kV). Particle-in-cell simulations performed in CST-PS and ICEPIC demonstrated very satisfactory agreement when compared with each other, and accurately predicted viable experimental performance at these op-

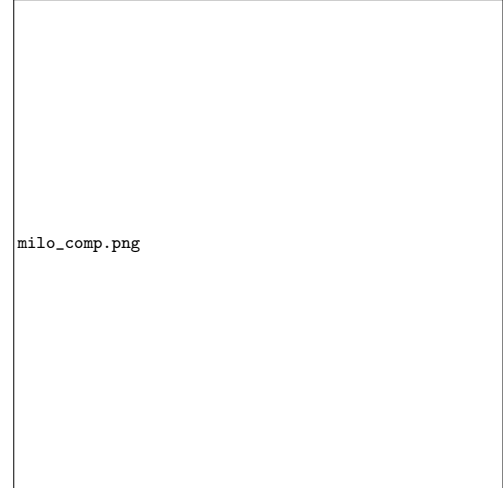


FIG. 15. Operating conditions from several MILO experiments, compared with HC,  $f_m$ ,  $f_u$ , and BH conditions from theory. (a) Voltage plotted against normalized flux, similar to the BH diagram<sup>5-7</sup> applied to magnetrons where the horizontal axis is the magnetic field. (b) Experimental flux ratio plotted against operating voltage, indicating the degree of magnetic insulation achieved in the experiments, with the solid red curve showing  $f_m$  and the dashed red curve showing  $f_u$ .

erating parameters. The theory revealed a novel operating state, where at constant voltage the total input current decreases as the diode is insulated slightly beyond the Hull cutoff condition in a v-shaped curve (Fig. 2a). While holding voltage constant as magnetic insulation is increased, the current reaches an absolute minimum before increasing monotonically (Fig. 2a). The MELBA experiments operated consistently in this v-shaped curve, magnetically insulated near the Hull cutoff condition rather than the Buneman-Hartree condition, and were corroborated by the simulations. Other devices, designed to operate at comparatively lower impedance ( $\sim 10 \Omega$ ) and higher current ( $\sim 30-50$  kA), showed proclivity for operation in this v-shaped curve as well.

The theory used in this paper is predicated on the assumption of the Brillouin flow state, which has been widely accepted in both the MILO and magnetron community. Here, it is rigorously applied to the MILO geometry, and in the design and in the interpretation of the experiments. Of note are the rigorous derivation of the Buneman-Hartree condition, and the revelation of several unexpected features. The results are largely consistent with the extensive experience with prior MILO experiments. The rigor in the model has enabled conception of a new class of MILO with voltages far from the traditional operating point typically discussed in the literature, and such a design would have been difficult to find with PIC simulation alone. This rigorous treatment advances MILO de-

TABLE III. Listed operating parameters for other MILO experiments.

Author	$r_a$ (cm)	$r_c$ (cm)	$r_a/r_c$	$v_{ph}/c$	$V_a$ (kV)	$I_a$ (kA)
Packard et al. (this paper)	2.5	0.7	3.6	0.286	240	9
Haworth et al. <sup>9</sup>	8.6	5.7	1.5	0.305	500	60
Eastwood et al. <sup>15</sup>	7.5	3.75	2	0.333	460	26
Cousin et al. <sup>16</sup>	4	2.5	1.6	0.281	400	30 <sup>a</sup>
Fan et al. <sup>10</sup>	9.3	6.6	1.4	0.433	530	60

<sup>a</sup> 31.75 kA is the minimum current  $I_a^{min}$  at this voltage (400 kV).

sign to a similar theoretical level as magnetron design, and the insights of this paper may be important to optimization of future MILOs by the community at large. In particular, the role of nonlinear saturation and loss of spoke charge and current to the walls may be important features in breaking the pure Brillouin flow that was assumed to make analytic progress, and this may explain various efficiency features seen by the wider MILO community. The appendix further examines the current distributions in a MILO and explores the efficiency issues.

#### ACKNOWLEDGMENTS

This work was supported in part by the U.S. Office of Naval Research through the Young Investigator Program and the Counter Directed Energy Weapons Program under Grants N00014-18-1-2499 and N00014-19-1-2262, and by the U.S. Air Force Office of Scientific Research under Awards FA9550-18-1-0153 and FA9550-20-1-0409. The coauthors would also like to thank the Air Force Research Laboratory for their support with ICEPIC, as well as the Directed Energy Professional Society for their graduate scholarship program.

#### DATA AVAILABILITY

The data that supports these findings may be made available by the corresponding author upon reasonable request.

#### Appendix

This appendix provides an elementary estimate of various current components in an operating MILO, based on the Brillouin flow model. Assume that the Brillouin hub current,  $I_e$ , gives rise to the spoke current,  $I_{spoke}$ , with the remaining part,  $(I_e - I_{spoke})$ , collected as a portion of the downstream diode current,  $I_d$ . Thus, including the cathode current  $I_c$ , the downstream diode current can be expressed as

$$I_d = I_c + (I_e - I_{spoke}). \quad (\text{A.1})$$

Copying Eq. (7) here for convenience,

$$I_a = I_c + I_e, \quad (\text{A.2})$$

together with Eq. (A.1) yields,

$$I_{spoke} = I_a - I_d. \quad (\text{A.3})$$

Equation (A.3) is essentially the slow wave structure current,  $I_{SWS}$ , that is constructed in Fig. (6). From Eqs. (9) and (13), the following can be obtained,

$$\frac{I_a}{I_c} = \cosh(\chi_b) = \gamma_b = 1 + \frac{V_b}{511 \text{ kV}} \quad (\text{A.4})$$

where  $V_b$  is the potential at the top of the Brillouin hub relative to the cathode<sup>25</sup>.

Next, assume a perfect energy conversion process, and a perfect output extractor, so that the total potential energy drop carried by the spoke electrons, from top of the Brillouin hub to the anode, is converted into RF power at the output. Then, the output power is given by,

$$P_{out} = I_{spoke}(V_a - V_b). \quad (\text{A.5})$$

These equations can be applied to the ICEPIC results from the  $r_d = 12$  mm case, which are shown in Fig. 6 and 7a, and listed below in Table A1. Using these parameters, Eq. (A.3) gives  $I_{spoke} = 1.99$  kA, which is the same as in Fig. 6. Equation (A.5) next yields  $V_b = 200$  kV, from which Eq. (A.4) yields  $I_c = 6.16$  kA. Finally, Eq. (A.2) gives  $I_e = 2.41$  kA. Note that  $I_{spoke}/I_e = 0.826$ , indicating that 82.6% of the electron current in the Brillouin hub is turned into spokes. Such a high fraction of spoke current in a MILO is in sharp contrast to magnetrons, once more because MILO operates close to Hull cutoff.

The above estimates are meant only to qualitatively illustrate the physics involved. The simple equations, (A.1)-(A.5), cannot be expected to completely embrace the complexities of MILO operation. One obvious deficiency is the assumption of a perfect extractor. If the extractor efficiency is included,  $\eta_{ex}$  ( $< 1$ ), Eq. (A.5) would be modified to read,

$$P_{out} = \eta_{ex} I_{spoke} (V_a - V_b). \quad (\text{A.6})$$

This change would materially affect all quantities. It is well-known that MILO performance is sensitive to the design of the output extractor<sup>9</sup>.

TABLE A1. MILO operating parameters obtained from an ICEPIC simulation.

$r_d$ (mm)	$V_a$ (kV)	$I_a$ (kA)	$I_d$ (kA)	$P_{out}$ (MW)
12	235	8.57	6.58	70

## REFERENCES

- <sup>1</sup>G. Bekefi and T. J. Orzechowski, "Giant Microwave Bursts Emitted from a Field-Emission, Relativistic-Electron-Beam Magnetron," *Physical Review Letters* **37**, 379–382 (1976).
- <sup>2</sup>O. Buneman, "A Toroidal Magnetron," *Proceedings of the Physical Society. Section B* **63**, 278–288 (1950).
- <sup>3</sup>R. W. Lemke and M. Collins Clark, "Theory and simulation of high-power microwave generation in a magnetically insulated transmission line oscillator," *Journal of Applied Physics* **62**, 3436–3440 (1987).
- <sup>4</sup>M. C. Clark, B. M. Marder, and L. D. Bacon, "Magnetically insulated transmission line oscillator," *Applied Physics Letters* **52**, 78–80 (1988).
- <sup>5</sup>J. Benford, J. Swegle, and E. Schamiloglu, *High Power Microwaves*, third edition ed. (CRC Press, Boca Raton, FL, 2016).
- <sup>6</sup>R. J. Barker, J. H. Booske, N. C. Luhmann Jr., and G. S. Nusinovich, *Modern Microwave and Millimeter-Wave Power Electronics* (Wiley, Piscataway, NJ, USA, 2005).
- <sup>7</sup>R. J. Barker and E. Schamiloglu, *High-Power Microwave Sources and Technologies* (IEEE Press, New York, NY, USA, 2001).
- <sup>8</sup>S. E. Calico, M. C. Clark, R. W. Lemke, and M. C. Scott, "Experimental and theoretical investigations of a magnetically insulated line oscillator (MILO)," in *Proc. SPIE*, edited by H. E. Brandt (San Diego, CA, 1995) pp. 50–59.
- <sup>9</sup>M. Haworth, G. Baca, J. Benford, T. Englert, K. Hackett, K. Hendricks, D. Henley, M. LaCour, R. Lemke, D. Price, D. Ralph, M. Sena, D. Shiffler, and T. Spencer, "Significant pulse-lengthening in a multigigawatt magnetically insulated transmission line oscillator," *IEEE Transactions on Plasma Science* **26**, 312–319 (1998).
- <sup>10</sup>F. Yu-Wei, S. Ting, L. Yong-Gui, Z. Hui-Huang, L. Zhi-Qiang, W. Yong, Z. Yan-Song, and L. Ling, "A Compact Magnetically Insulated Line Oscillator with New-Type Beam Dump," *Chinese Physics Letters* **22**, 164–167 (2005).
- <sup>11</sup>D.-B. Chen, D. Wang, F.-B. Meng, and Z.-K. Fan, "Bifrequency Magnetically Insulated Transmission Line Oscillator," *IEEE Transactions on Plasma Science* **37**, 23–29 (2009).
- <sup>12</sup>J. Benford, "History and future of the relativistic magnetron," in *2010 International Conference on the Origins and Evolution of the Cavity Magnetron* (IEEE, Bournemouth, United Kingdom, 2010) pp. 40–45.
- <sup>13</sup>D. Andreev, A. Kuskov, and E. Schamiloglu, "Review of the relativistic magnetron," *Matter and Radiation at Extremes* **4**, 067201 (2019).
- <sup>14</sup>A. W. Hull, "The Effect of A Uniform Magnetic Field on the Motion of Electrons Between Coaxial Cylinders," *Phys. Review* **18**, 32 (1921).
- <sup>15</sup>J. Eastwood, K. Hawkins, and M. Hook, "The tapered MILO," *IEEE Transactions on Plasma Science* **26**, 698–713 (1998).
- <sup>16</sup>R. Cousin, J. Larour, J. Gardelle, B. Cassany, P. Modin, P. Gouard, and P. Raymond, "Gigawatt Emission From a 2.4-GHz Compact Magnetically Insulated Line Oscillator (MILO)," *IEEE Transactions on Plasma Science* **35**, 1467–1475 (2007).
- <sup>17</sup>F. Yu-Wei, Z. Hui-Huang, L. Zhi-Qiang, S. Ting, Y. Han-Wu, Y. Jian-Hua, W. Yong, L. Ling, and Z. Yan-Song, "Investigation of an X-band magnetically insulated transmission line oscillator," *Chinese Physics B* **17**, 1804–1808 (2008).
- <sup>18</sup>Y. Fan, X. Wang, G. Li, H. Yang, H. Zhong, and J. Zhang, "Experimental Demonstration of a Tunable Load-Limited Magnetically Insulated Transmission Line Oscillator," *IEEE Transactions on Electron Devices* **63**, 1307–1311 (2016).
- <sup>19</sup>X. Wang, Y. Fan, T. Shu, B. Yang, X. Xu, A. Li, Z. Liu, and H. Xu, "Experimental Demonstration of a Ridged Magnetically Insulated Transmission Line Oscillator," *IEEE Transactions on Microwave Theory and Techniques* **69**, 1698–1702 (2021).
- <sup>20</sup>R. M. Gilgenbach, L. D. Horton, R. F. Lucey, S. Bidwell, M. Cuneo, J. Miller, and L. Smutek, "Microsecond Electron Beam Diode Closure Experiments," in *Invited Talk, Proceedings of the IEEE Pulsed Power Conference* (Crystal City, VA, 1985) p. 7.
- <sup>21</sup>Y.-W. Fan, H.-H. Zhong, Z.-Q. Li, T. Shu, H.-W. Yang, H. Zhou, C.-W. Yuan, W.-H. Zhou, and L. Luo, "Repetition rate operation of an improved magnetically insulated transmission line oscillator," *Physics of Plasmas* **15**, 083102 (2008).
- <sup>22</sup>F. Qin, D. Wang, S. Xu, Y. Zhang, and Z.-k. Fan, "Repetitive operation of an L-band magnetically insulated transmission line oscillator with metal array cathode," *Review of Scientific Instruments* **87**, 044703 (2016).
- <sup>23</sup>Y. Y. Lau, D. A. Packard, C. J. Swenson, J. W. Luginsland, D. Li, A. Jassem, N. M. Jordan, and R. M. Gilgenbach, "Explicit Brillouin flow solutions in magnetrons, magnetically insulated line oscillators, and radial magnetically insulated transmission lines," *IEEE Trans. Plasma Sci.* (2021), 10.1109/TPS.2021.3092606.
- <sup>24</sup>R. M. Gilgenbach, Y.-Y. Lau, D. M. French, B. W. Hoff, J. Luginsland, and M. Franzl, "Crossed field device," (Sep. 2014), US Patent No. 8,841,867 B2.
- <sup>25</sup>Y. Y. Lau, J. W. Luginsland, K. L. Cartwright, D. H. Simon, W. Tang, B. W. Hoff, and R. M. Gilgenbach, "A re-examination of the Buneman-Hartree condition in a cylindrical smooth-bore relativistic magnetron," *Physics of Plasmas* **17**, 033102 (2010).
- <sup>26</sup>R. D. McBride, W. A. Stygar, M. E. Cuneo, D. B. Sinar, M. G. Mazarakis, J. J. Leckbee, M. E. Savage, B. T. Hutsel, J. D. Douglass, M. L. Kiefer, B. V. Oliver, G. R. Laity, M. R. Gomez, D. A. Yager-Elorriaga, S. G. Patel, B. M. Kovalchuk, A. A. Kim, P.-A. Gourdain, S. N. Bland, S. Portillo, S. C. Bott-Suzuki, F. N. Beg, Y. Maron, R. B. Spielman, D. V. Rose, D. R. Welch, J. C. Zier, J. W. Schumer, J. B. Greenly, A. M. Covington, A. M. Steiner, P. C. Campbell, S. M. Miller, J. M. Woolstrum, N. B. Ramey, A. P. Shah, B. J. Sporer, N. M. Jordan, Y. Y. Lau, and R. M. Gilgenbach, "A Primer on Pulsed Power and Linear Transformer Drivers for High Energy Density Physics Applications," *IEEE Transactions on Plasma Science* **46**, 3928–3967 (2018).
- <sup>27</sup>D. Packard, *Innovative Crossed-Field Devices for the Generation of High Power Microwaves*, Doctoral Dissertation, University of Michigan, Ann Arbor, MI, USA (2021).
- <sup>28</sup>R. Lemke, S. Calico, and M. Clark, "Investigation of a load-limited, magnetically insulated transmission line oscillator (MILO)," *IEEE Transactions on Plasma Science* **25**, 364–374 (1997).
- <sup>29</sup>H. Zhou, T. Shu, and Z.-q. Li, "Investigation of a high impedance magnetically insulated transmission line oscillator with hollow load," *Physics of Plasmas* **19**, 093113 (2012).
- <sup>30</sup>P. J. Christenson and Y. Y. Lau, "Transition to turbulence in a crossed-field gap," *Physics of Plasmas* **1**, 3725–3727 (1994); Erratum, **3**, 4293 (1996).
- <sup>31</sup>M. Lopez, Y. Y. Lau, J. W. Luginsland, D. W. Jordan, and R. M. Gilgenbach, "Limiting current in a relativistic diode under the condition of magnetic insulation," *Physics of Plasmas* **10**, 4489–4493 (2003).
- <sup>32</sup>J. Slater, *Microwave Electronics* (D. Van Norstrand Company, 1950).
- <sup>33</sup>D. A. Packard, A. Cooleybeck, N. M. Jordan, B. J. Sporer, A. E. Mazarakis, Y. Y. Lau, R. M. Gilgenbach, and R. D. McBride, "HFSS and CST Simulations of a GW-Class MILO," *IEEE Transactions on Plasma Science* **48**, 1894–1901 (2020).
- <sup>34</sup>Z. Cendes, "The development of HFSS," in *2016 UNSC-URSI Radio Science Meeting* (IEEE, Fajardo, PR, USA, 2016) pp. 39–40.
- <sup>35</sup>M. C. Balk, "Simulation possibilities of vacuum electronic devices with CST PARTICLE STUDIO," in *2008 IEEE International Vacuum Electronics Conference* (IEEE, Monterey, CA, USA, 2008) pp. 459–460.
- <sup>36</sup>R. Peterkin and J. Luginsland, "A virtual prototyping environment for directed-energy concepts," *Computing in Science & Engineering* **4**, 42–49 (2002).
- <sup>37</sup>C. Wilsen, J. Luginsland, Y. Lau, T. Antonsen, D. Chermn, P. Tchou, M. Keyser, R. Gilgenbach, and L. Ludeking, "A simulation study of beam loading on a cavity," *IEEE Transactions on Plasma Science* **30**, 1160–1168 (2002).
- <sup>38</sup>A. Taflov, S. C. Hagness, and M. Picket-May, "Computational Electromagnetics: The Finite-Difference Time-Domain Method," in *The Electrical Engineering Handbook* (Elsevier, 2005) pp. 629–670.
- <sup>39</sup>J.-P. Berenger, "A perfectly matched layer for the absorption of electromagnetic waves," *Journal of Computational Physics* **114**, 185–200 (1994).

This is the author's peer reviewed, accepted manuscript. However, the online version of record will be different from this version once it has been copyedited and typeset.

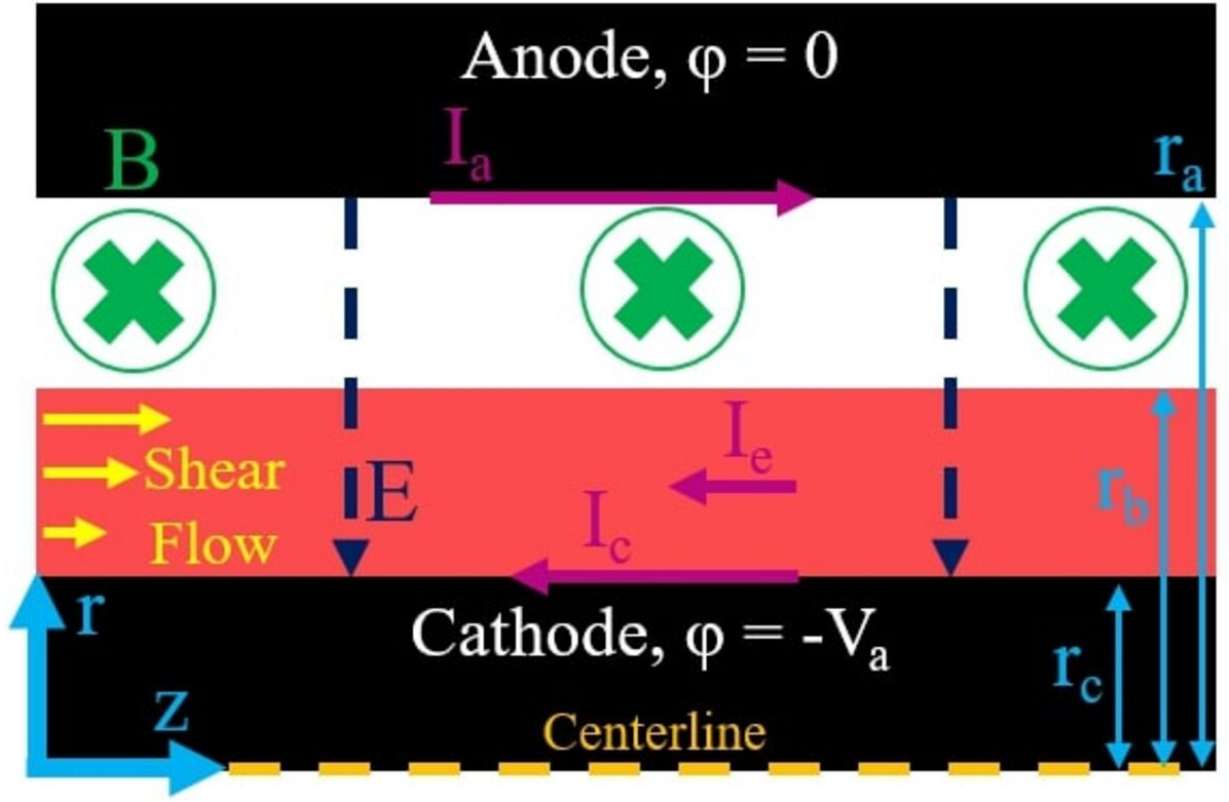
PLEASE CITE THIS ARTICLE AS DOI: 10.1063/5.0071455

- <sup>40</sup>M. D. Haworth, T. J. Englert, K. J. Hendricks, R. W. Lemke, J. W. Luginsland, D. S. Shiffler, and T. A. Spencer, "Comprehensive diagnostic suite for a magnetically insulated transmission line oscillator," *Review of Scientific Instruments* **71**, 1539–1547 (2000).
- <sup>41</sup>Y.-w. Fan, H.-h. Zhong, Z.-q. Li, C.-w. Yuan, T. Shu, H.-w. Yang, Y. Wang, and L. Luo, "Investigation of a 1.2-GHz Magnetically Insulated Transmission Line Oscillator," *IEEE Transactions on Plasma Science* **39**, 540–544 (2011).
- <sup>42</sup>M. I. Fuks and E. Schamiloglu, "Application of a magnetic mirror to increase total efficiency in relativistic magnetrons," *Physical Review Letters* **122**, 224801 (2019).
- <sup>43</sup>Y.-W. Fan, X.-Y. Wang, Z.-C. Zhang, T. Xun, and H.-W. Yang, "A high-efficiency repetitively pulsed magnetically insulated transmission line oscillator," *Vacuum* **128**, 39–44 (2016).
- <sup>44</sup>X. Wang, Y. Fan, T. Shu, A. Li, Y. Yu, and Z. Liu, "A High-Efficiency Magnetically Insulated Transmission Line Oscillator With Ridged Disk-Loaded Vanes," *IEEE Trans. Plasma Sci.* **47**, 4 (2019).
- <sup>45</sup>A. D. Greenwood, "An ICEPIC Convergence Study Using a Relativistic Magnetron," AFRL Technical Memorandum , 18 (2005).
- <sup>46</sup>M. A. Franzl, *Relativistic Recirculating Planar Magnetrons*, Doctoral Dissertation, University of Michigan, Ann Arbor, MI, USA (2014).
- <sup>47</sup>K. Hendricks and M. Haworth, "Experiments on high-power microwave transmission through a belljar," *IEEE Transactions on Plasma Science* **30**, 1215–1219 (2002).
- <sup>48</sup>M. Lopez, R. Gilgenbach, M. Jones, W. White, D. Jordan, M. Johnston, T. Strickler, V. Neculaes, Y. Lau, T. Spencer, M. Haworth, K. Cartwright, P. Mardahl, J. Luginsland, and D. Price, "Relativistic Magnetron Driven by a Microsecond E-Beam Accelerator With a Ceramic Insulator," *IEEE Transactions on Plasma Science* **32**, 1171–1180 (2004).
- <sup>49</sup>D. Price and J. N. Benford, "General Scaling of Pulse Shortening in Explosive-Emission-Driven Microwave Sources," *IEEE Trans. Plasma Sci.* **26**, 7 (1998).
- <sup>50</sup>Fen Qin, Dong Wang, Dai-Bing Chen, and Zhi-Kai Fan, "Simulation Investigation of L-Band Ladder Cathode MILO," *IEEE Transactions on Plasma Science* **37**, 1921–1924 (2009).
- <sup>51</sup>G. Dixit and B. Singh, "Study on Load-Side Optimization in Bifrequency MILO Source," *IEEE Transactions on Plasma Science* **48**, 3552–3557 (2020).
- <sup>52</sup>M. Haworth, K. Cartwright, J. Luginsland, D. Shiffler, and R. Umstadtd, "Improved electrostatic design for milo cathodes," *IEEE Transactions on Plasma Science* **30**, 992–997 (2002).
- <sup>53</sup>E. C. Okress, *Crossed-Field Microwave Devices* (Academic Press, New York, NY, USA, 1961).
- <sup>54</sup>R. Cousin, J. Larour, P. Gouard, and P. Raymond, "Evidence of the  $3\pi/4$  interaction mode in a compact magnetically insulated line oscillator process," *Journal of Applied Physics* **100**, 084512 (2006).



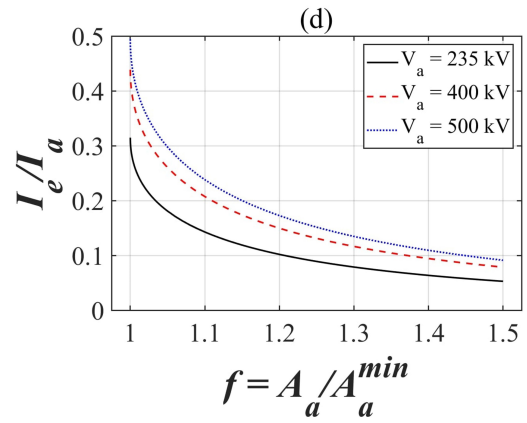
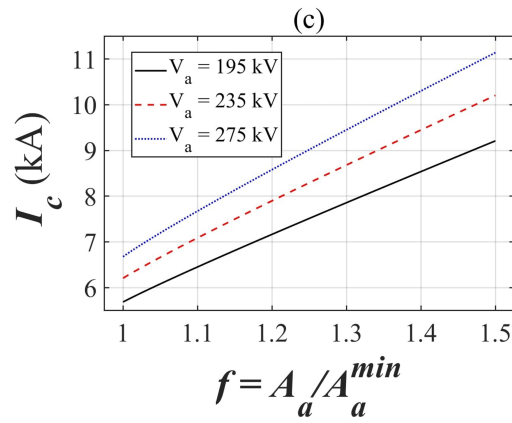
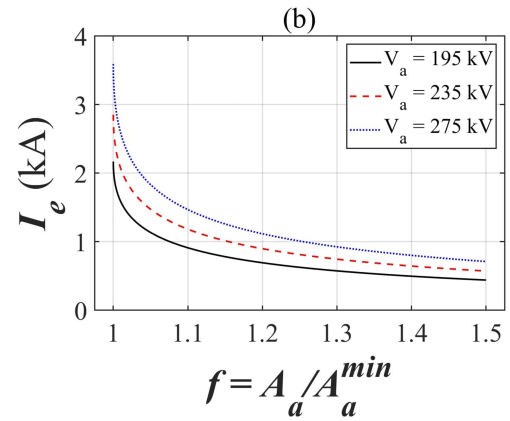
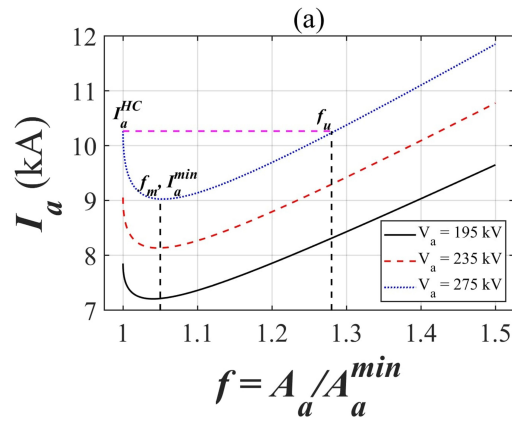
This is the author's peer reviewed, accepted manuscript. However, the online version of record will be different from this version once it has been copyedited and typeset.

PLEASE CITE THIS ARTICLE AS DOI: 10.1063/1.50071455



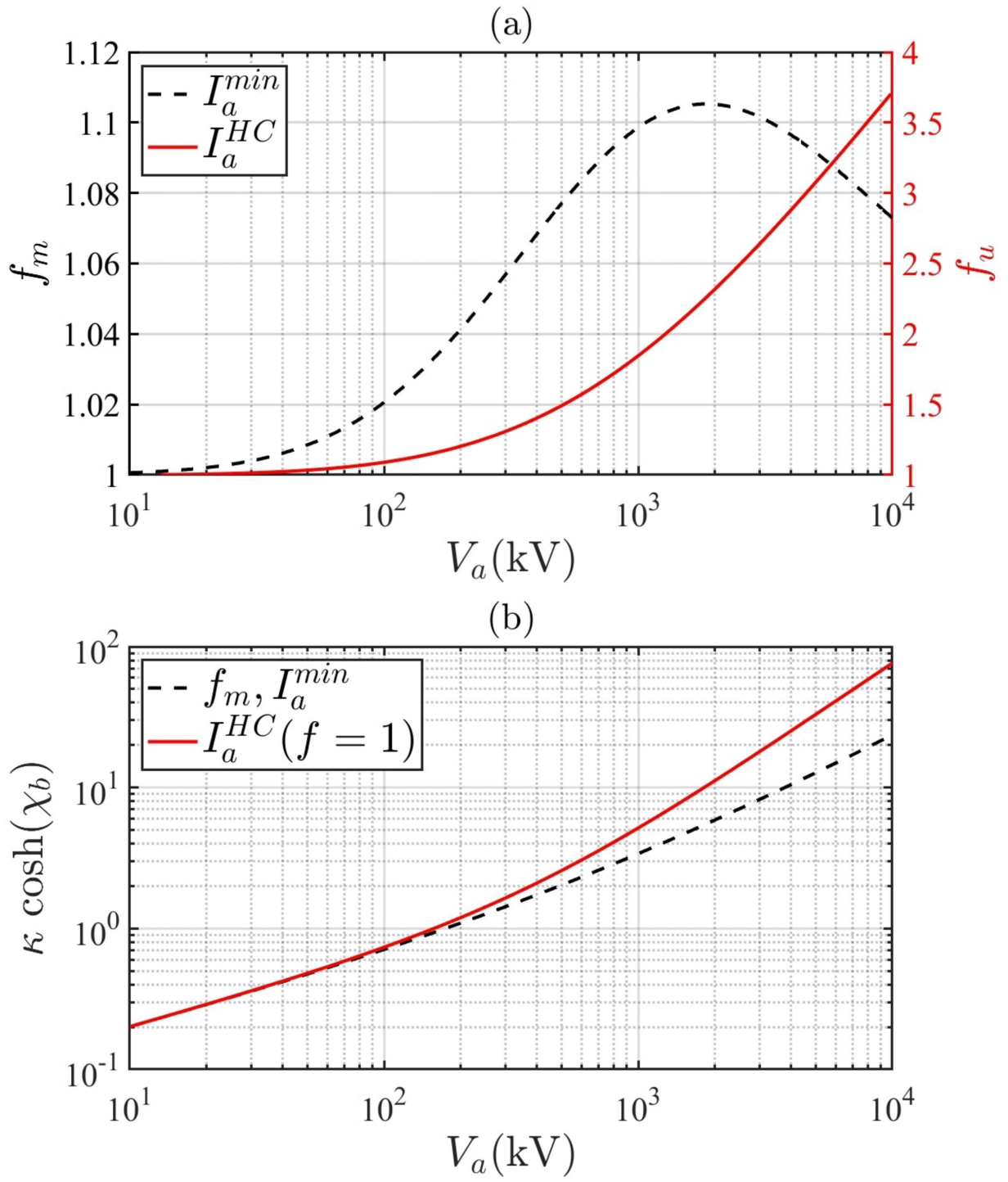
This is the author's peer reviewed, accepted manuscript. However, the online version of record will be different from this version once it has been copyedited and typeset.

PLEASE CITE THIS ARTICLE AS DOI: 10.1063/5.0071455

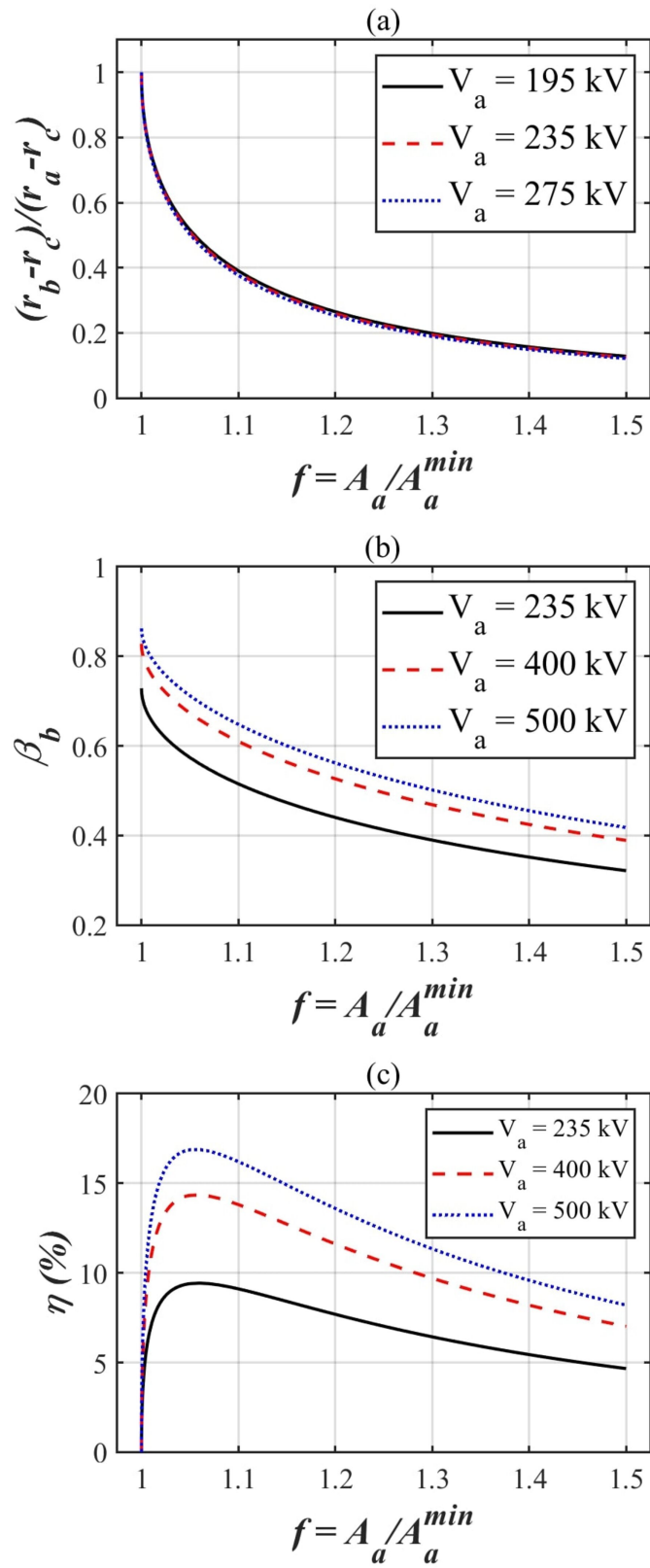


This is the author's peer reviewed, accepted manuscript. However, the online version of record will be different from this version once it has been copyedited and typeset.

PLEASE CITE THIS ARTICLE AS DOI: 10.1063/5.0071455

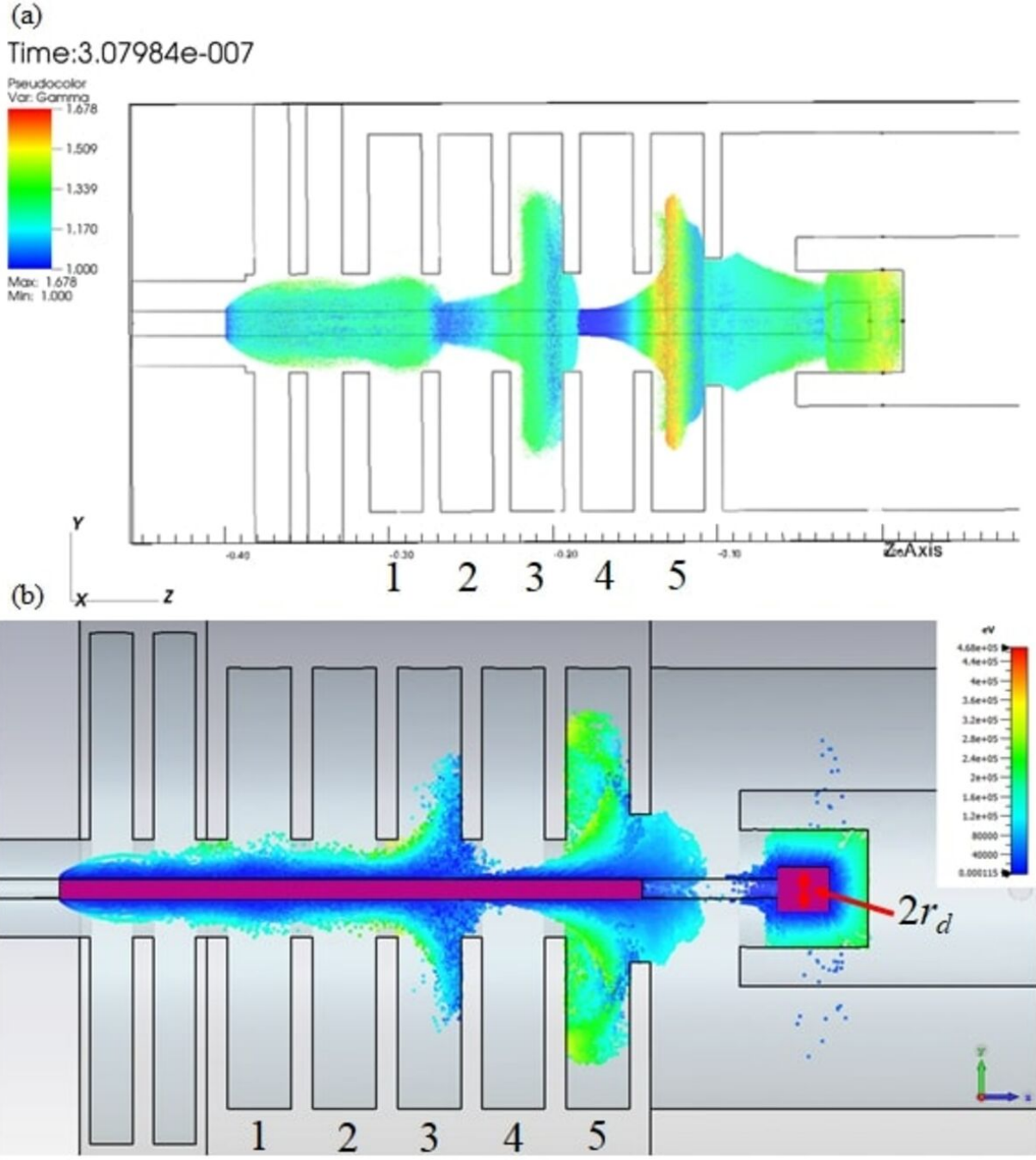


This is the author's peer reviewed, accepted manuscript. However, the online version of record will be different from this version once it has been copyedited and typeset.  
 PLEASE CITE THIS ARTICLE AS DOI: 10.1063/1.50071455



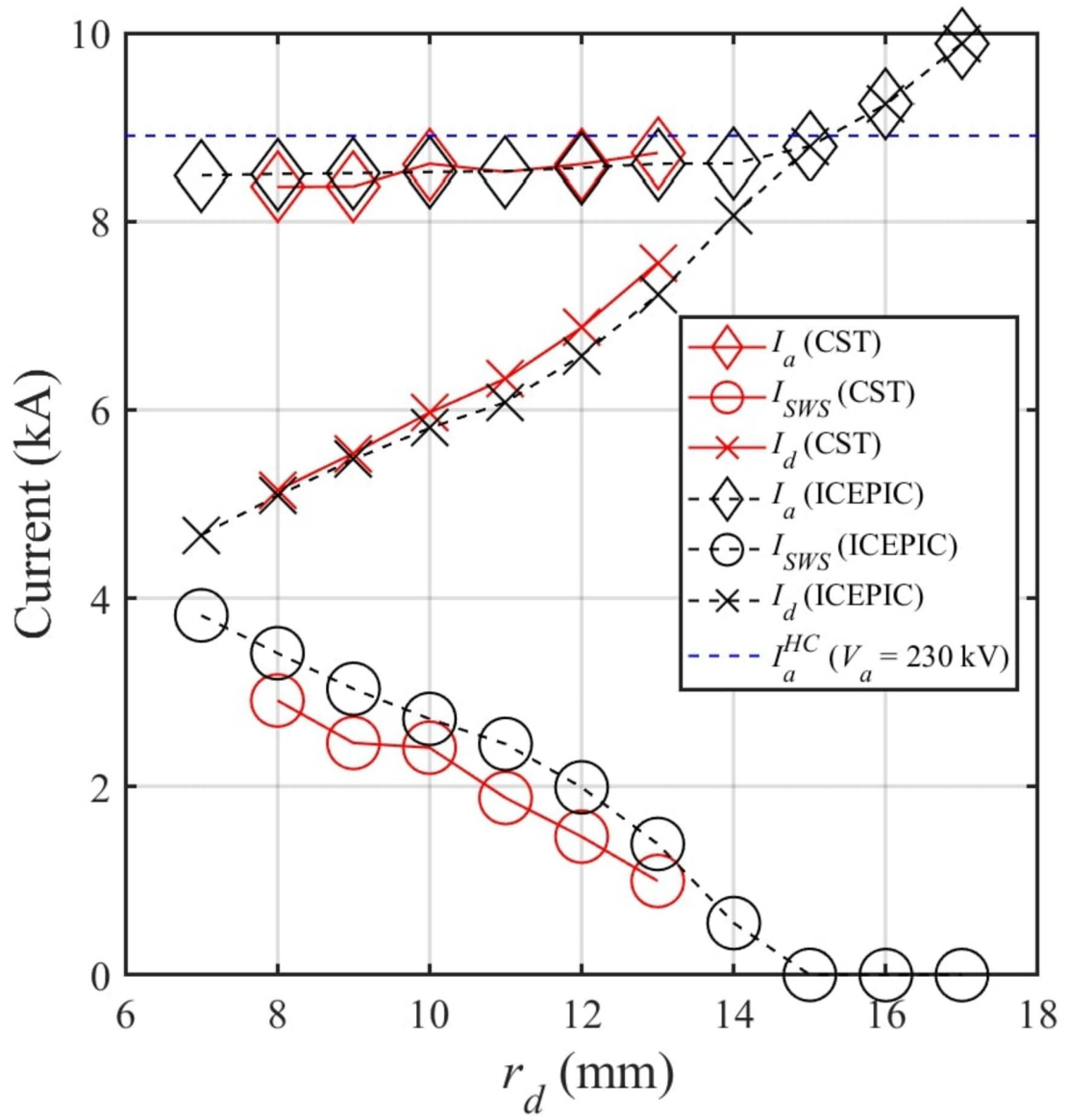
This is the author's peer reviewed, accepted manuscript. However, the online version of record will be different from this version once it has been copyedited and typeset.

PLEASE CITE THIS ARTICLE AS DOI: 10.1063/1.50071455



This is the author's peer reviewed, accepted manuscript. However, the online version of record will be different from this version once it has been copyedited and typeset.

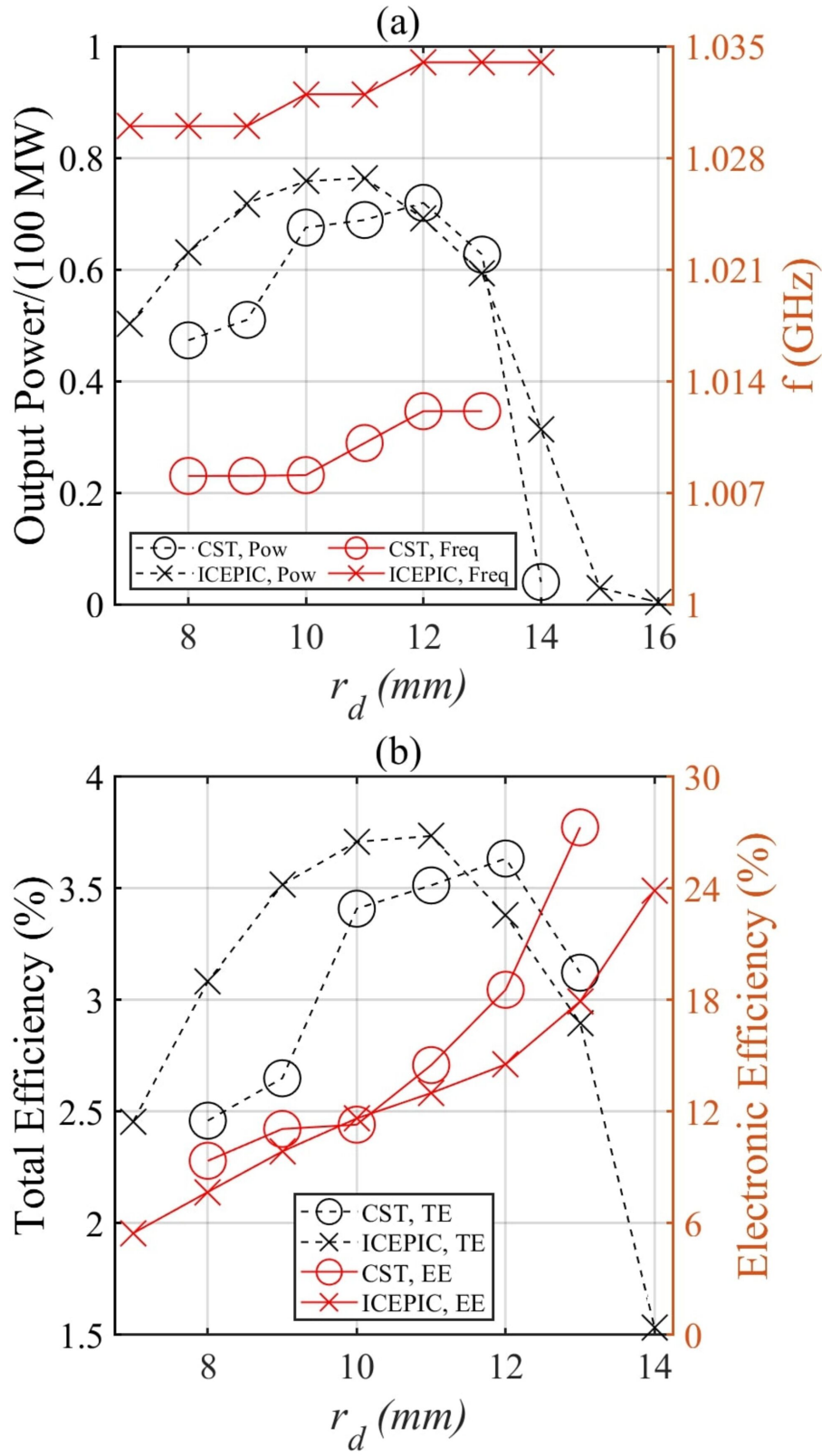
PLEASE CITE THIS ARTICLE AS DOI: 10.1063/1.50071455





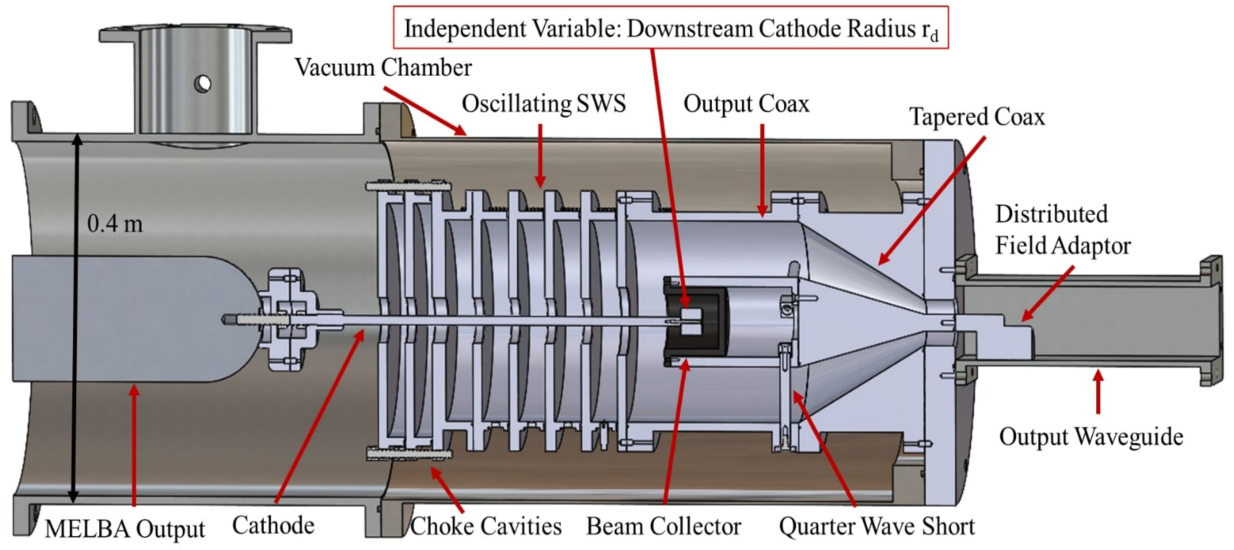
This is the author's peer reviewed, accepted manuscript. However, the online version of record will be different from this version once it has been copyedited and typeset.

PLEASE CITE THIS ARTICLE AS DOI: 10.1063/5.0071455



This is the author's peer reviewed, accepted manuscript. However, the online version of record will be different from this version once it has been copyedited and typeset.

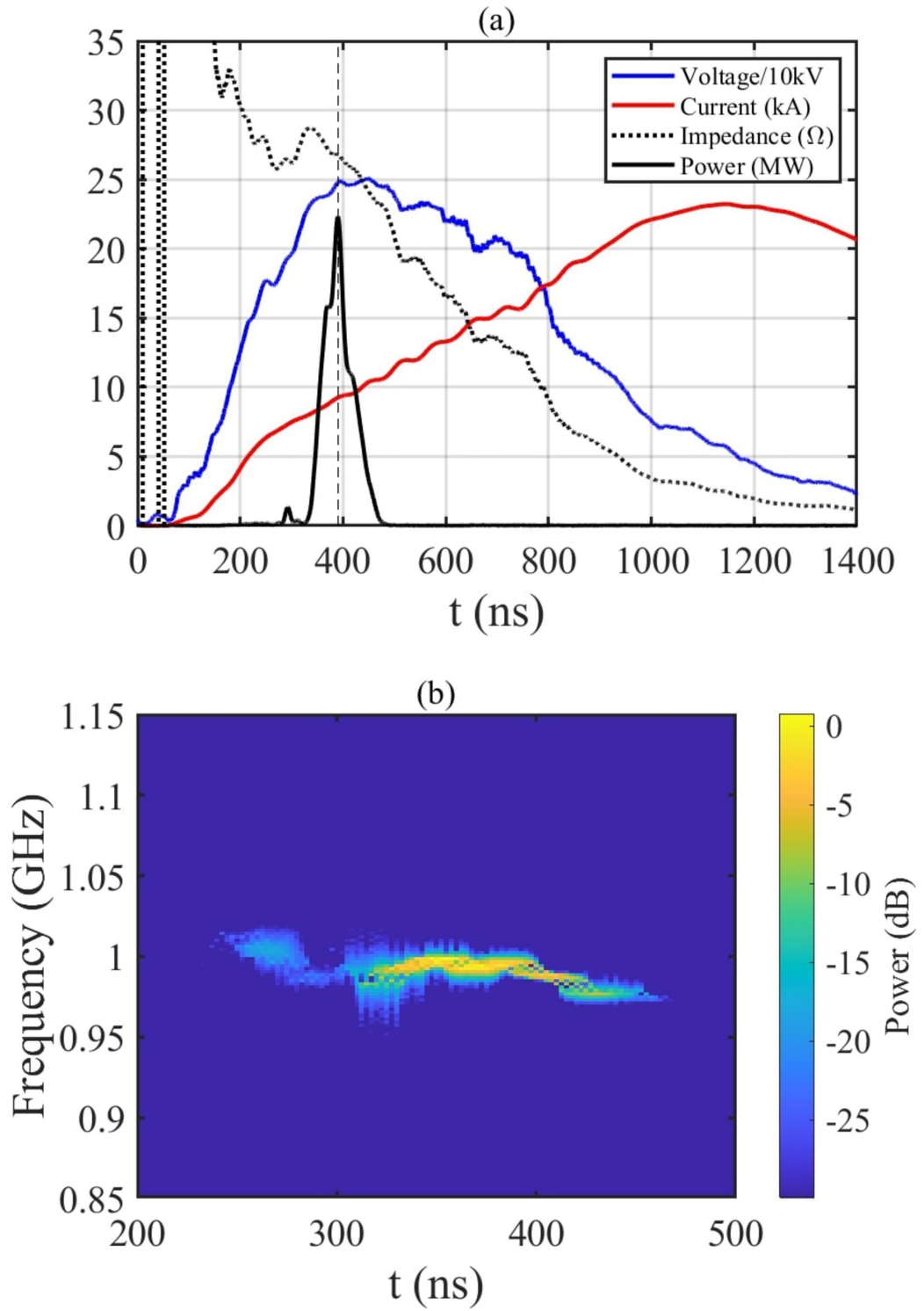
PLEASE CITE THIS ARTICLE AS DOI: 10.1063/5.0071455



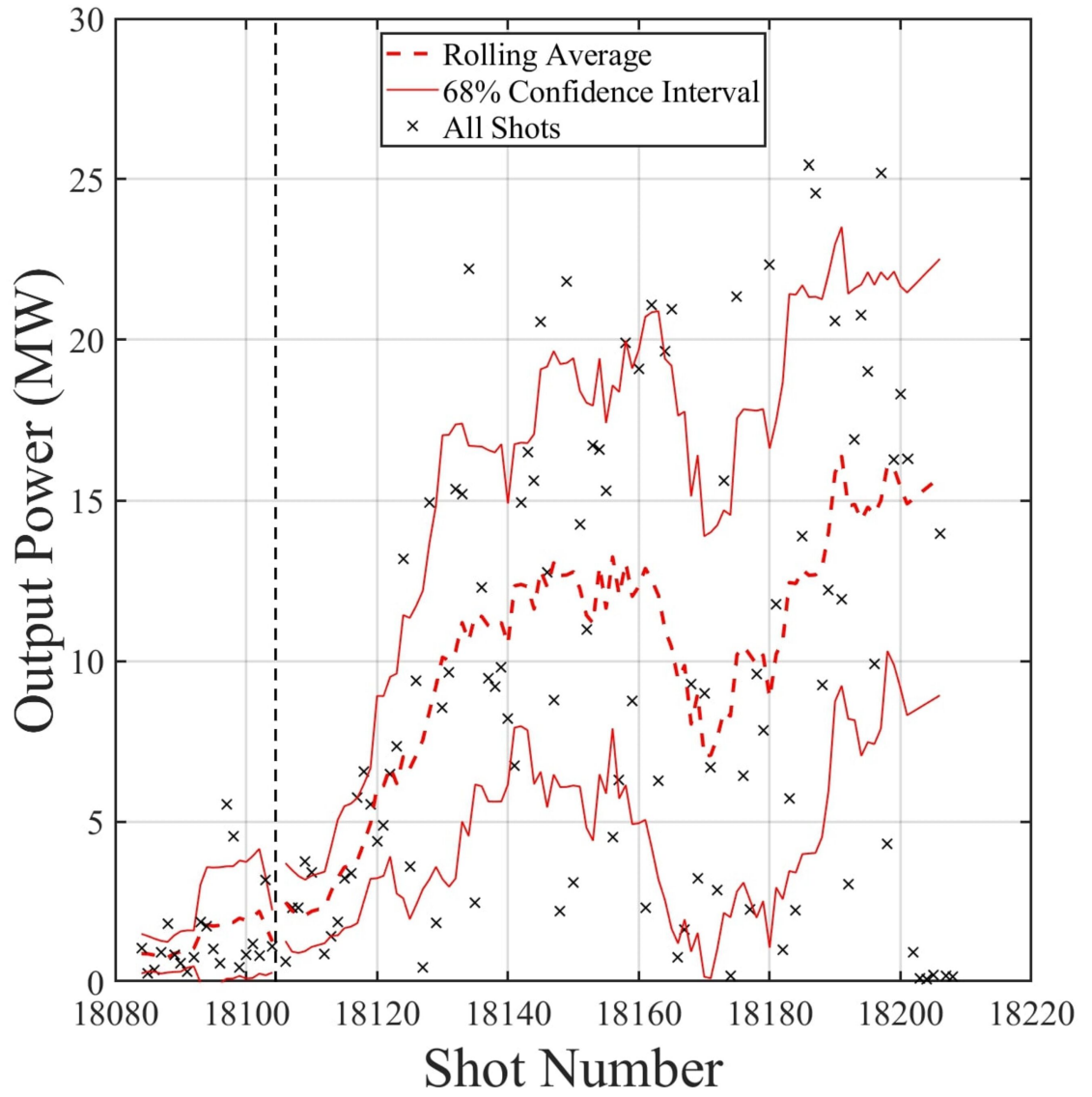


This is the author's peer reviewed, accepted manuscript. However, the online version of record will be different from this version once it has been copyedited and typeset.

PLEASE CITE THIS ARTICLE AS DOI: 10.1063/5.0071455

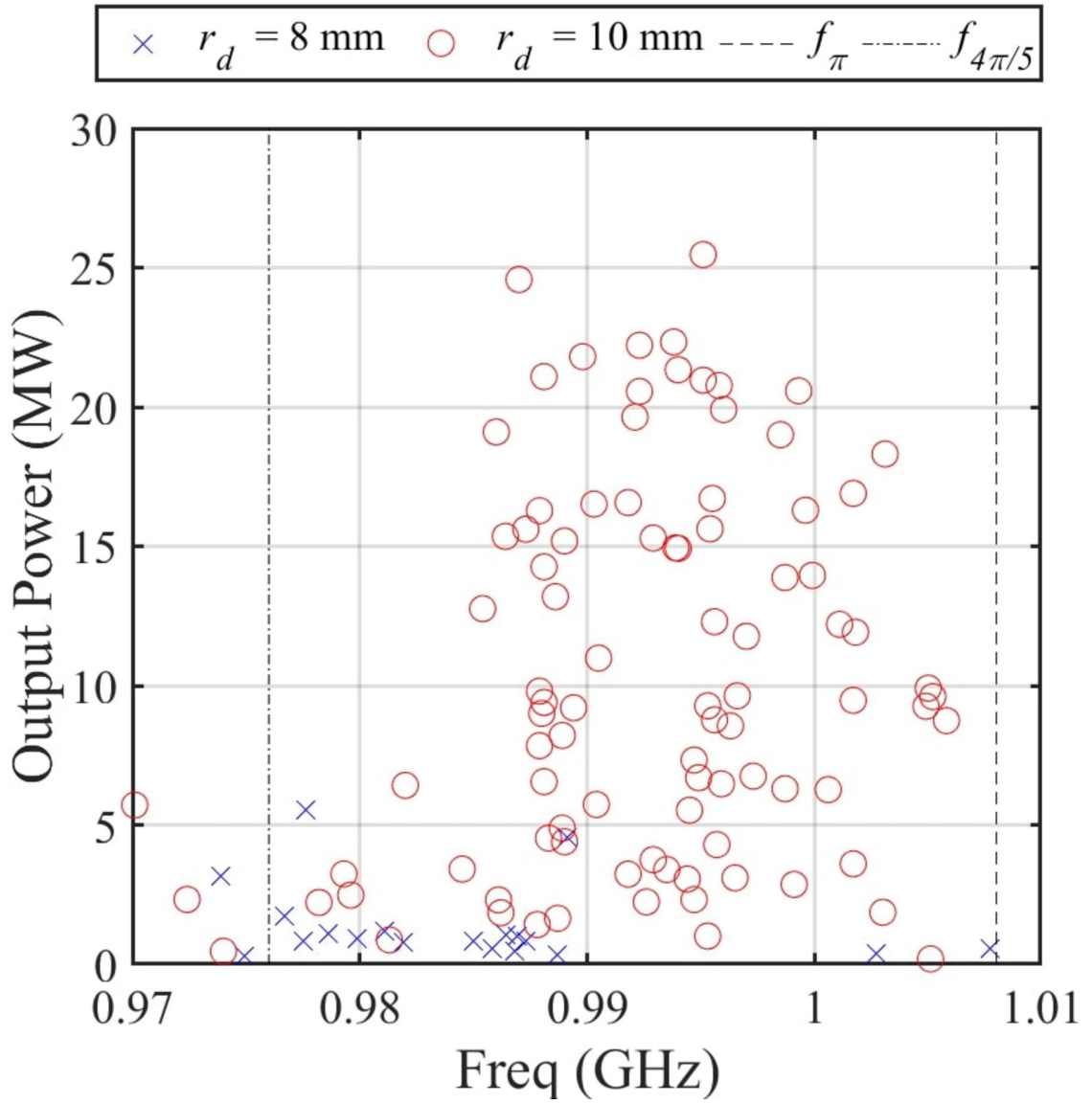


This is the author's peer reviewed, accepted manuscript. However, the online version of record will be different from this version once it has been copyedited and typeset.  
 PLEASE CITE THIS ARTICLE AS DOI: 10.1063/5.0071455



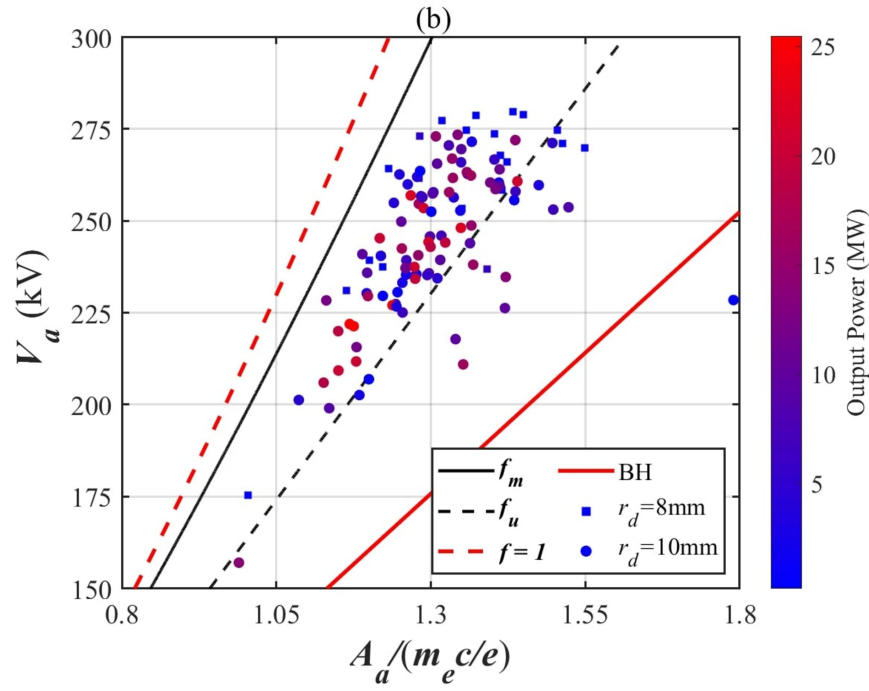
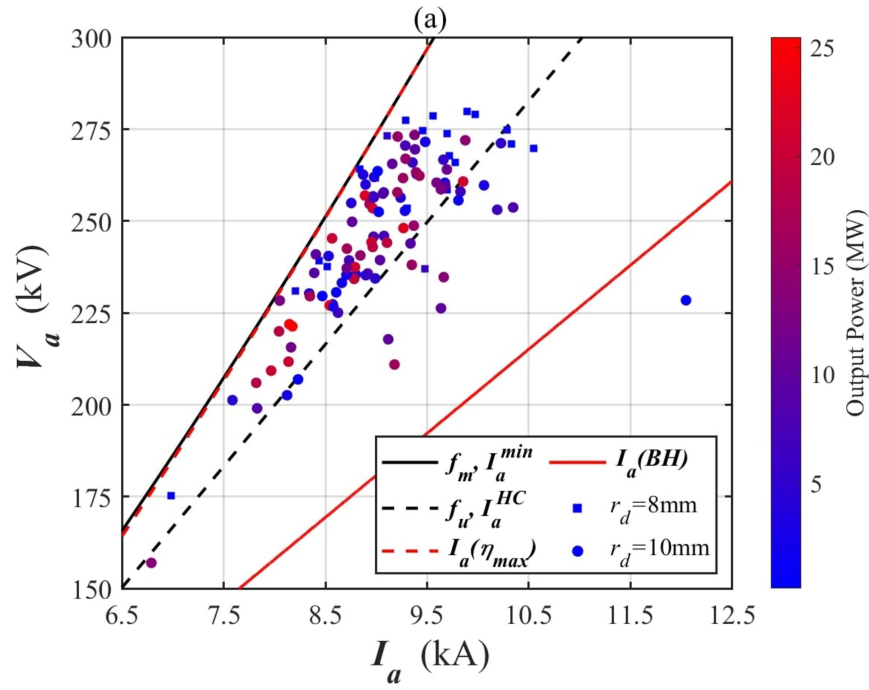
This is the author's peer reviewed, accepted manuscript. However, the online version of record will be different from this version once it has been copyedited and typeset.

PLEASE CITE THIS ARTICLE AS DOI: 10.1063/5.0071455



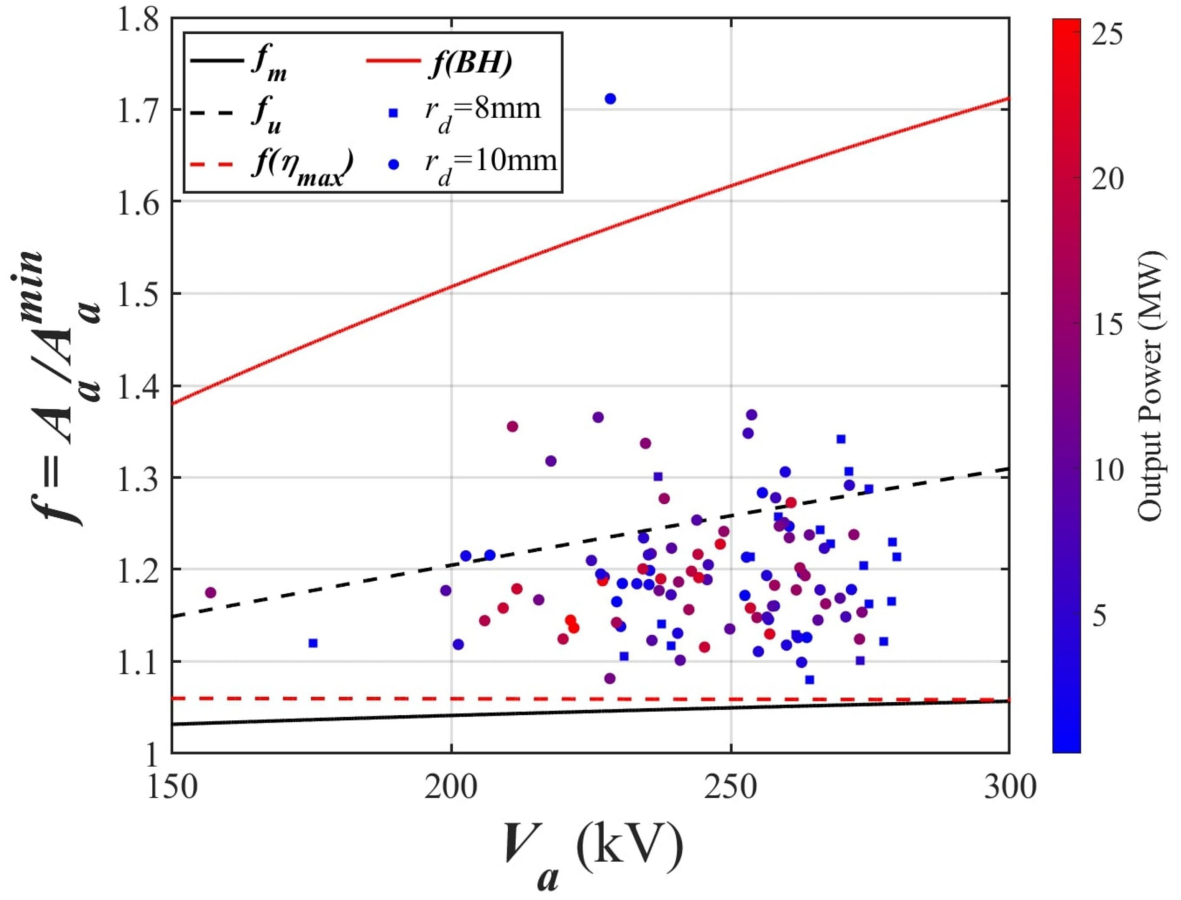
This is the author's peer reviewed, accepted manuscript. However, the online version of record will be different from this version once it has been copyedited and typeset.

PLEASE CITE THIS ARTICLE AS DOI: 10.1063/5.0071455



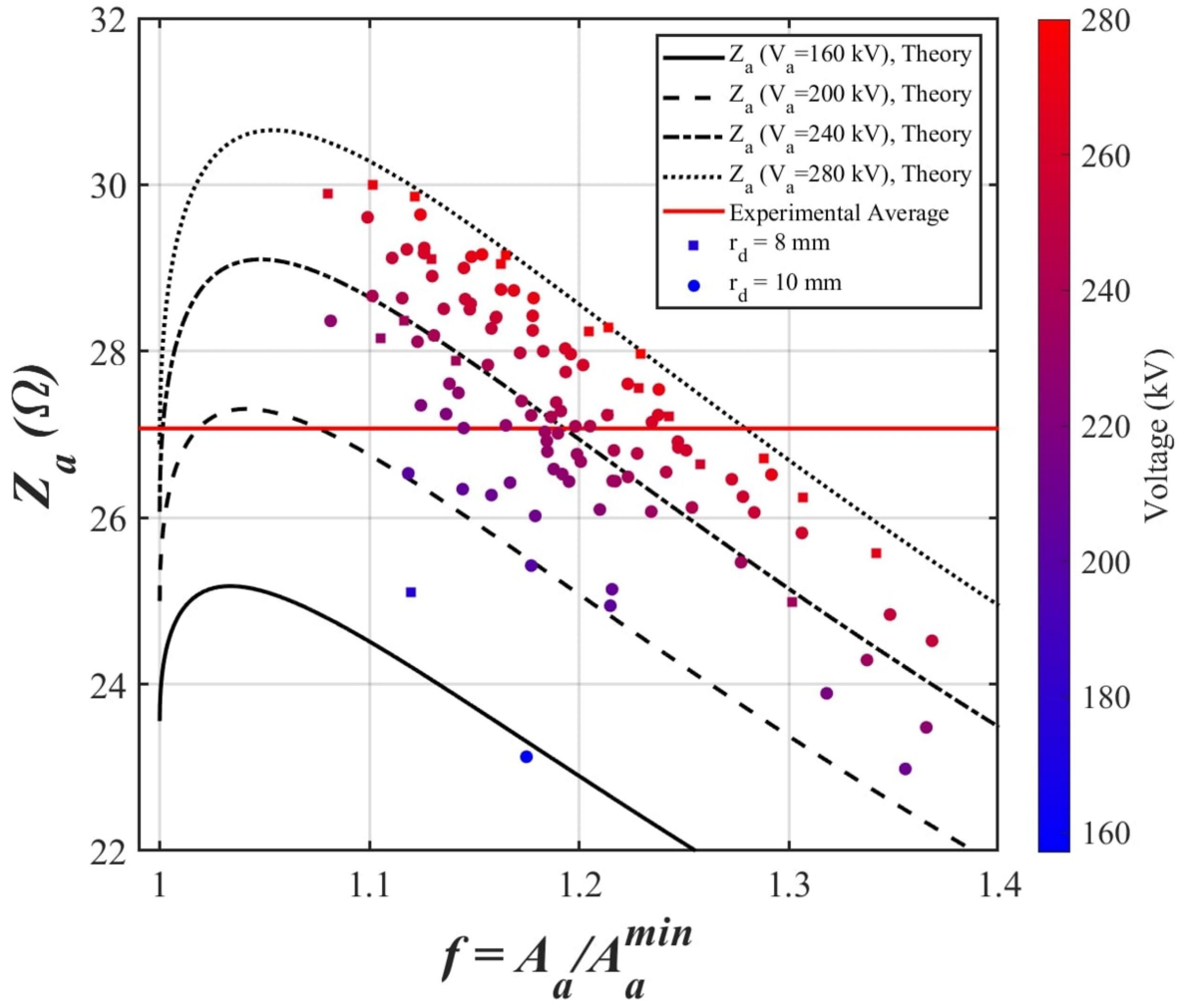
This is the author's peer reviewed, accepted manuscript. However, the online version of record will be different from this version once it has been copyedited and typeset.

PLEASE CITE THIS ARTICLE AS DOI: 10.1063/5.0071455



This is the author's peer reviewed, accepted manuscript. However, the online version of record will be different from this version once it has been copyedited and typeset.

PLEASE CITE THIS ARTICLE AS DOI: 10.1063/5.0071455



This is the author's peer reviewed, accepted manuscript. However, the online version of record will be different from this version once it has been copyedited and typeset.

PLEASE CITE THIS ARTICLE AS DOI: 10.1063/1.50071455

